The deep OB star population in Carina from the VST Photometric Hα Survey (VPHAS+)

M. Mohr-Smith,[1] J. E. Drew,[1]★ R. Napiwotzki,[1] S. Simón-Díaz,[2,3] N. J. Wright,[1,4]
G. Barentsen,[1,5] J. Eislöffel,[6] H. J. Farnhill,[1] R. Greimel,[7] M. Monguió,[1]
V. Kalari,[8] Q. A. Parker[9] and J. S. Vink[10]

[1]*Centre for Astrophysics Research, Science and Technology Research Institute, University of Hertfordshire, Hatfield AL10 9AB, UK*
[2]*Instituto de Astrofísica de Canarias, E-38200 La Laguna, Tenerife, Spain*
[3]*Departamento de Astrofísica, Universidad de La Laguna, E-38205 La Laguna, Tenerife, Spain*
[4]*Astrophysics Group, Keele University, Keele ST5 5BG, UK*
[5]*NASA Ames Research Center, Moffatt Field, Mountain View, CA 94043, USA*
[6]*Thüringer Landessternwarte Tautenburg, Sternwarte 5, D-07778 Tautenburg, Germany*
[7]*Department for Geophysics, Institute of Physics, Astrophysics and Meteorology, NAWI Graz, Universitätsplatz 5, A-8010 Graz, Austria*
[8]*Departamento de Astronomía, Universidad de Chile, Camino El Observatorio 1515, Las Condes, Santiago, Casilla 36-D, Chile*
[9]*Department of Physics, The University of Hong Kong, Pokfulam Road, Hong Kong, China*
[10]*Armagh Observatory, College Hill, Armagh BT61 9DG, Northern Ireland*

ABSTRACT

Massive OB stars are critical to the ecology of galaxies and yet our knowledge of OB stars in the Milky Way, fainter than $V \sim 12$, remains patchy. Data from the VST Photometric Hα Survey (VPHAS+) permit the construction of the first deep catalogues of blue excess-selected OB stars, without neglecting the stellar field. A total of 14 900 candidates with 2MASS cross-matches are blue-selected from a 42 deg^2 region in the Galactic plane, capturing the Carina Arm over the Galactic longitude range $282° \lesssim \ell \lesssim 293°$. Spectral energy distribution fitting is performed on these candidates' combined VPHAS+ *u*, *g*, *r*, *i* and 2MASS *J*, *H*, *K* magnitudes. This delivers effective temperature constraints, statistically separating O from early-B stars and high-quality extinction parameters, A_0 and R_V (random errors typically $\sim$0.1). The high-confidence O-B2 candidates number 5915 and a further 5170 fit to later B spectral type. Spectroscopy of 276 of the former confirms 97 per cent of them. The fraction of emission-line stars among all candidate B stars is 7–8 per cent. Greyer ($R_V > 3.5$) extinction laws are ubiquitous in the region, over the distance range 2.5–3 to $\sim$10 kpc. Near prominent massive clusters, R_V tends to rise, with particularly large and chaotic excursions to $R_V \sim 5$ seen in the Carina Nebula. The data reveal a hitherto unnoticed association of 108 O-B2 stars around the O5If+ star LSS 2063 ($\ell = 289°.77$, $b = -1°.22$). Treating the OB star scaleheight as a constant within the thin disc, we find an orderly mean relation between extinction (A_0) and distance in the Galactic longitude range, $287°.6 < \ell < 293°.5$, and infer the subtle onset of thin-disc warping. A halo around NGC 3603, roughly a degree in diameter, of $\sim$500 O-B2 stars with $4 < A_0(\mathrm{mag}) < 7$ is noted.

Key words: surveys – stars: early-type – dust, extinction – Galaxy: disc – open clusters and associations: general.

1 INTRODUCTION

Massive OB stars are critically important objects in shaping the evolution of galactic environments. But because of their relative rarity due to the initial mass function (IMF) and their short lives, they have proved to be difficult to nail down in terms of their evolution before and after the main sequence (MS): their formation is still subject to debate (Tan et al. 2014) and we cannot say with any certainty what exact fate awaits which type of massive object (Langer 2012). It has long been recognized that the UV radiation and supernovae they produce are huge factors in shaping the interstellar medium (ISM).

★ E-mail: j.drew@herts.ac.uk

As things stand, the best-studied resolved massive star population can be claimed to be located in the Magellanic Clouds, thanks to the VLT-FLAMES Tarantula Survey (Evans et al. 2011, and subsequent papers) that produced a coherent spectroscopic data set of over 800 massive stars. This survey captured well the properties of a population of massive stars at reduced metallicity ([Fe/H] $\simeq -0.3$). In contrast, the impact of varying levels of significant extinction renders the higher metallicity disc of our own galaxy more of a challenge. Existing catalogues of the O and early-B stars are confined to objects brighter than $\sim$12th magnitude (complete only to $\sim$2 kpc; see e.g. Garmany, Conti & Chiosi 1982) and are heterogeneous (e.g. Reed 2003). An effort is underway to collect complete spectroscopy of the known bright Galactic O-star population (GOSSS by Maíz Apellániz et al. 2011, and subsequent papers) but, limited by the source material it presently rests on, only a few tens of objects have yet been covered over the range $12 < B < 16$ (Maíz Apellániz et al. 2016). So far, the known fainter reddened OB stars are mostly located in massive clusters that are more easily noticed against the Galactic background.

There is thus a gap in our knowledge of the wider field population: this presents a problem to the debate over the significance of the runaway phenomenon (Portegies Zwart, McMillan & Gieles 2010) and how this should be tensioned against the possibility of forming massive stars outside densely clustered environments (de Wit et al. 2005; Bressert et al. 2012). Furthermore, as we await the arrival of advanced astrometry from ESA's *Gaia* mission, it is the perfect time to trace how OB stars fit into the structure of the star-forming Galactic thin disc, reaching well beyond the solar neighbourhood. Mapping these intrinsically luminous objects is important for another reason: they have long been valued as distant and bright backlighters of the ISM – much of what is known about interstellar extinction has been deduced from fitting the spectral energy distributions (SEDs) of OB stars (e.g. Cardelli, Clayton & Mathis 1989; Fitzpatrick & Massa 2007; Maíz Apellániz et al. 2014). A new deep census of OB stars has much to offer.

The cheapest method of astronomical census is provided by photometry. At the time Johnson & Morgan (1953) introduced the *UBV* photometric system, they also described the concept of exploiting the $(U - B, B - V)$ colour–colour (CC) diagram to construct reddening-free parameters labelling reddening lines for distinct stellar spectral subtypes. This introduced a method of analysing stellar photometry that can now be applied with greatly increased power to very large, homogeneous data sets in this new era of survey photometry. It works especially well as a tool to select hot massive OB stars: the aim of this paper is to apply a customized version of it to newly minted data from the VST[1] Photometric Hα Survey of the Southern Galactic Plane and Bulge (VPHAS+; Drew et al. 2014). The target region for this work, intended both as an upscaling of our already validated method and as an exploration of a part of the Milky Way particularly rich in massive OB stars, is the Carina region of the Galactic plane.

In a previous paper (Mohr-Smith et al. 2015), we presented a first blue selection from VPHAS+ data that focused on a region spanning just 2 deg^2, around the massive O-star-rich cluster, Westerlund 2. This adapted the method of reddening-free parameters to the Sloan filter system in use at the VST and performed a validation test on a catalogue of objects that had been selected from the $(u - g, g$

$- r)$ diagram, and further winnowed through fitting u, g, r, i and published J, H, K magnitudes to progressively reddened synthetic stellar photometry. The haul from this was a list of 489 objects with spectral types of B2 or earlier – most of them were new discoveries, representing an order of magnitude increase on the total known from previous catalogues.

It became clear in this first pilot that the characterization of extinction is particularly high in quality: the typical precisions achieved are 0.1 in each of A_0, the monochromatic extinction in magnitudes at 4595 Å and R_V, the ratio of total to selective extinction. The new, expanded catalogue of candidate OB stars included both discoveries within Westerlund 2 and a handful of similarly reddened O stars scattered around it at offsets of between 10 and 40 arcmin. The latter may have been ejected from the cluster or they may be evidence of a wider star-forming event within which Westerlund 2 is the most prominent feature. To settle this, spectroscopic follow-up is required. The new work here expands the sky area from 2 deg^2 up to 42 and the number of high-confidence candidate O–B2 stars from 489 to 5915.

The total footprint spanning the Carina Nebula and environs is shown in Fig. 1: it runs from close to the Carina arm tangent direction, at $\ell \sim 282°$ (Dame 2007; Vallée 2014) through Westerlund 2 and on through the Carina Nebula, to beyond the brilliant massive open cluster, NGC 3603, ending at $\ell \simeq 293°$. The irregular footprint outline, with reduced latitude coverage at lower longitudes, reflects the processed data available at the outset of this work. The longitude range examined is much the same as that investigated by Graham (1970) who used Walraven photometry to map 436 bright ($8.5 \lesssim V \lesssim <11.5$) OB stars. Indeed, the work we present amounts to an update, almost 50 years on, which reaches from 10 to more than 1000 times fainter.

On the map of Galactic spiral arm structure presented by Russeil (2003), the Carina Arm is the single most compelling and coherent feature. In CO maps (Grabelsky et al. 1987; Dame, Hartmann & Thaddeus 2001), the arm is traceable as a somewhat broken ridge of emission that has a near side about 2 kpc away, running from higher Galactic longitude to the tangent point 4–6 kpc distant (see the discussion by Dame 2007): it connects to the far side beyond the tangent as it carries on unwinding out beyond the Solar Circle: Grabelsky et al. (1987) suggested heliocentric distances of the order 10–12 kpc for the arm at $\ell \sim 293°$. The famous Carina Nebula is generally regarded as being embedded in the near portion of the arm, 2.5–3 kpc away (Tapia et al. 2003; Hur, Sung & Bessell 2012; Kumar et al. 2014), while NGC 3603 is associated with the far arm, $\sim$7 kpc away (Sung & Bessell 2004). It aids visualization of the arm to notice that 11° of longitude corresponds to roughly 1.1 kpc at $\sim$5 kpc distance – not much of a bend over the potential heliocentric distance range to $\sim$10 kpc. Nevertheless, a little curvature, turbulent motions and recent star formation create complexity in the dust distribution that demands high-density sightline sampling.

This paper is organized as follows: the first major section, Section 2, presents the photometry and how it is exploited to select and characterize the optically fainter Carina OB-star population; the results of the selection are presented in Section 3 along with exercises aiming to distinguish the minority of non-MS objects included in it; the quality of the selection is then examined more closely in Section 4 by analysing follow-up spectroscopy of a subset of candidates located within a single field 2° in diameter as marked on Fig. 1. The outcome is that almost all the high-confidence candidates are confirmed. Finally, in Section 5, the new catalogue of 5915 candidate OB stars is used in an appraisal of the trends in extinction (A_0) and extinction law (R_V) across the studied region. We then

---

[1] The VST is the VLT Survey Telescope and the VLT is the Very Large Telescope, a set of four 8-m telescopes operated by the European Southern Observatory (ESO).
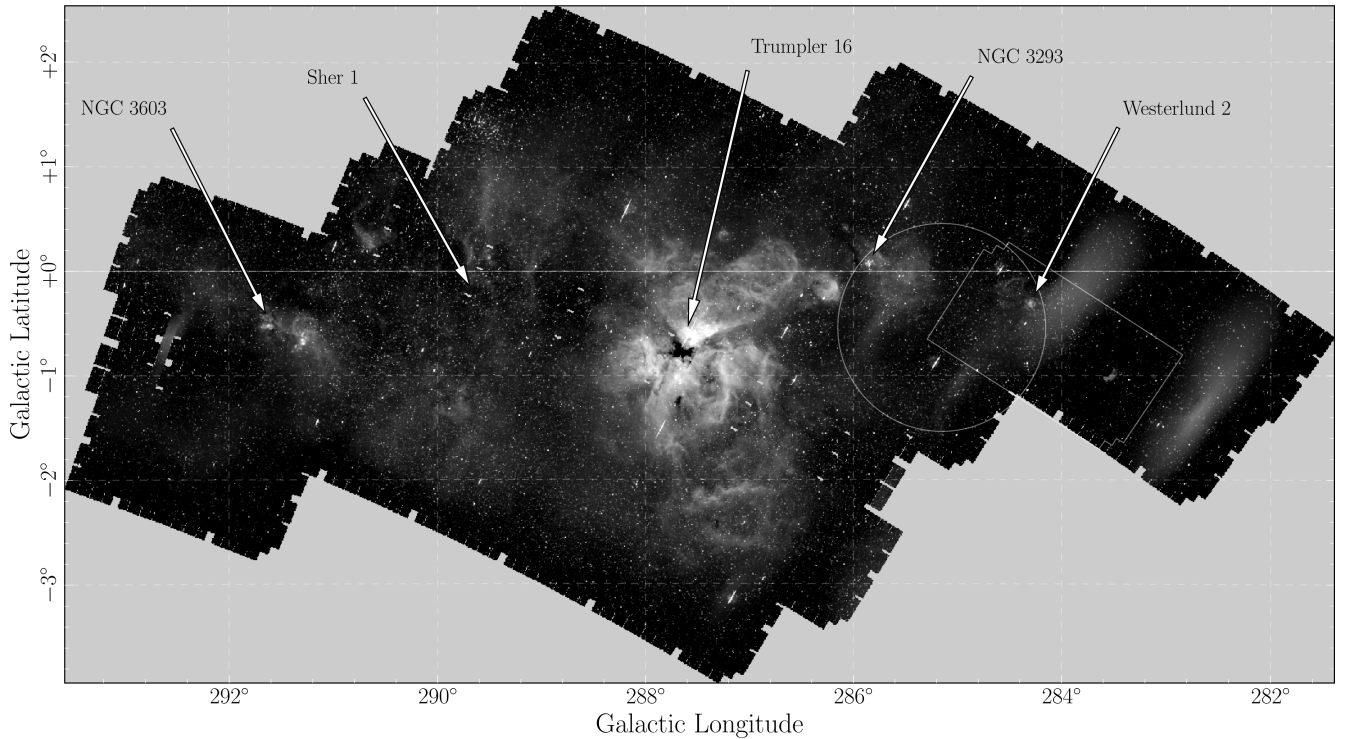
Figure 1. VPHAS+ Hα image showing the footprint of the 42 deg² in Carina that are studied here. The positions of some major OB star clusters are labelled. The white rectangle shows the area studied in (Mohr-Smith et al. 2015) and the circle shows the area studied with spectroscopy in Section 4. The two large bright smudges in the far right, and that on the far left of the footprint are due to scattered light in the constituent images that are not pipeline-corrected for illumination effects (which are included in the photometric catalogue generation).

experiment with adopting the OB-star scaleheight within the thin disc as a standard ruler in order to set a scale to the rise in extinction with heliocentric distance. This works over the longitude range $287°\!.6 < \ell < 293°\!.5$ and leads in turn to measures of the onset of the warp of the Galactic thin disc. The paper ends with some discussion and the main conclusions in Section 6.

2 METHOD: THE OPTICAL PHOTOMETRY; OB-STAR SELECTION AND SED FITTING

2.1 VPHAS+ optical photometry

The optical photometry we exploit is from the VPHAS+ survey (described in full by Drew et al. 2014). This survey of the southern Galactic plane began at the end of 2011 and, at the time of writing, continues to execute on the VST at the Paranal site in Chile. The VST camera, OmegaCam, delivers 1×1 deg² images of the sky at a typical seeing of 0.8–0.9 arcsec in the Sloan *gri* and narrow-band Hα filters, rising to 1.0–1.1 arcsec in Sloan *u*. In all bands, the limiting (Vega) magnitude is typically greater than 20th, reaching as faint as 22nd in *g*. All data from the survey are pipeline-reduced to source lists, calibrated against nightly standards, by the Cambridge Astronomical Survey Unit (CASU). These are used in this study in the form of band-merged *ugr* and *ri*Hα contemporaneous catalogues. We note that the blue and the red filters are usually observed months apart – the repeated *r*-band observations are in place to serve as basic checks on variability. The raw materials for this study are the collated source catalogues for a set of 42 survey fields spanning the chosen Carina Galactic plane region (Fig. 1).

A new feature of expanding to the larger set of fields is that it is even more important to impose a uniform photometric calibration

Table 1. Mean zero-point calibration shifts in each broad-band and the standard deviations of repeated detections in overlaps, before and after adjustment to bring all fields on to a common photometric scale.

Band	Mean zero-point shift	σ_m before	σ_m after
u	0.38	0.029	0.027
g	0.04	0.030	0.015
r, Hα	0.09	0.027	0.019
i	0.07	0.028	0.024

across all the data. To achieve this, we have made comparisons on a field-by-field basis with *g*-, *r*- and *i*-band stellar photometry from the AAVSO Photometric All-Sky Survey and have then used the main stellar locus in the $(u - g, g - r)$ CC diagram to determine the *u*-band shifts required. The Hα band data are tied to the *r*-band calibration by requiring the Hα photometric zero-point to be offset from the *r* zero-point by 3.08. The details of this alignment process will be presented in a future presentation of VPHAS+ data products (Drew et al., in preparation). The mean photometric adjustments made to the broad-band data, as a result of these comparisons, are given in Table 1. The sense of all the tabulated shifts is such that the revised magnitude scale is brighter than the unrevised. In this paper, we express all magnitudes in the Vega system.

We have exploited the field overlaps provided by the tiling pattern of VPHAS+ (see Drew et al. 2014) in order to check the final uniformity of the recalibration. Within the overlap regions, it is possible for a star to have up to four independently recalibrated detections in each band. Using these, we can evaluate the convergence to a common scale by comparing the standard deviation of multiple measurements before and after the calibration adjustments.
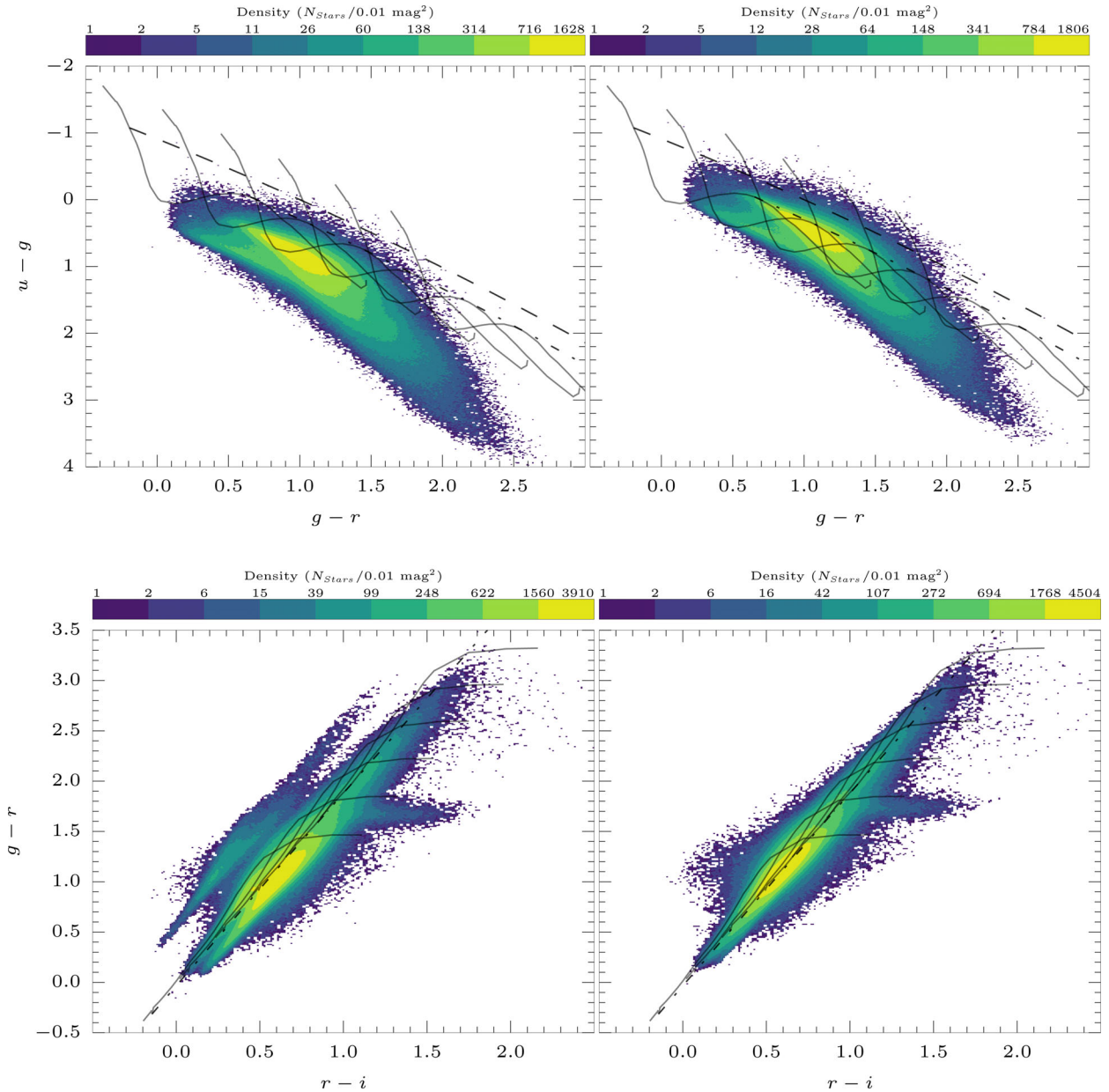
Figure 2. CC density plots showing the position of the main stellar locus with respect to the synthetic MS ($A_0 = 0$–10 mag in steps of 2) before (left) and after (right) recalibration. The dash–dotted line shows the G0V reddening vector while the dashed line shows the B3V reddening vector. The left lower panel clearly shows the presence of poorly calibrated exposures that are brought into line by our calibration corrections. The main correction of the upper left panel is an upward shift in $u - g$ linked to a systematic brightening of the u-band data (see Table 1).

These are set out, for the broad-bands, in Table 1: there is noticeable improvement in all of them and especially in g.

As the final confirmation of the improved uniformity of the data, after correction, we show in Fig. 2 before and after source density plots of the ($u - g$, $g - r$) and ($r - i$, $g - r$) CC diagrams for the region studied here. We can see that the diagrams have much tighter distributions with less scatter after correcting the individual field calibrations. The main stellar locus (highest density of sources) is also placed in the correct position with respect to the synthetic tracks. The data in Table 1, alongside Fig. 2, show that the main consequence of the u recalibration is to bring this band into better (astrophysical) alignment with the longer wavelength bands, rather than to reduce scatter. For the successful selection of candidate OB stars, this is critical.

2.2 OB-star selection and SED fitting

The methods for the selection of candidate OB stars and SED fitting are the same as those used and described in full by Mohr-Smith et al. (2015). Below, we summarize the main features.

2.2.1 Photometric selection and cross-matching

First, a ($u - g$, $g - r$) CC diagram is constructed that includes all catalogued objects with $g \leq 20$, a u detection and random photometric magnitude errors below 0.1 in g, r and i. OB stars in this diagram are offset above the main stellar locus and can be selected using a method related to the well-established Q method of Johnson & Morgan (1953). We select targets blueward of the B3V

reddening vector, i.e. above it, as drawn in the $(u - g, g - r)$ CC diagram in Fig. 2 (see also fig. 3 in Mohr-Smith et al. 2015). This aims at picking out all objects earlier than B3 (our target group). The number of objects in this initial selection was 37 971.

All candidates are then cross-matched against the Two Micron All-Sky Survey (2MASS), the only available near-infrared (NIR) survey covering the whole region. The maximum cross-match distance was set to 1 arcsec in forming optical near-infrared (OnIR) SEDs. As long as the NIR magnitudes of the initially selected objects are within the 2MASS range, the cross-matching is very successful since the VPHAS+ survey astrometry is calculated with reference to 2MASS. The 90th percentile cross-match separation is 0.3 arcsec and the median is 0.073 arcsec. Only objects with catalogued magnitudes in all seven bands (u, g, r, i, J, H, Ks) are retained for input into the SED fitting procedure.

2.2.2 SED fitting

We compare the empirical SEDs to a parametrized model in a simple Bayesian scheme using Markov Chain Monte Carlo (MCMC) sampling. The model consists of four parameters $\log(T_{\text{eff}})$, A_0, R_V and μ, the distance modulus. The intrinsic SEDs are taken from the Padova isochrone data base (CMD v2.2;[2] Bertelli et al. 1994; Bressan et al. 2012). As the OnIR colours of OB stars do not vary significantly with luminosity class or metallicity (Martins & Plez 2006), only MS, solar-metallicity models have been considered ($\log(g) \sim 4$, $Z = 0.019$). The models are then reddened using a set of Fitzpatrick & Massa (2007) reddening laws and shifted according to the distance modulus. As the apparent OnIR SEDs of OB stars change only subtly as a function of effective temperature (Martins & Plez 2006), the shape of their SEDs is controlled mainly by extinction. This means that $\log(T_{\text{eff}})$ is relatively weakly constrained, whilst permitting reasonable O/B separation (see Section 4). The extinction parameters, on the other hand, are well-constrained. As there is no luminosity class discrimination, μ acts primarily as a normalization factor and is highly correlated with effective temperature (see fig. 6 of Mohr-Smith et al. 2015).

The likelihood function used in the Bayesian scheme is a multivariate Gaussian that embeds the assumption that the uncertainties on all measurements/parameters are uncorrelated.[3] This reduces to the familiar sum for χ^2:

$$P(SED_{\text{obs}} \mid \theta) \propto \exp\left(-\frac{1}{2}\sum_i^n \frac{(m(obs)_i - m(mod)_i)^2}{\sigma_i^2}\right), \quad (1)$$

where $P(SED_{\text{obs}}|\theta)$ is the probability of obtaining the observed SED (SED_{obs}) given a set of parameters θ, and where $m(obs)_i$ and $m(mod)_i$ are the observed and model magnitudes in each band i. In this equation only, i is just a summation index

We have adopted uniform priors on each parameter which are as follows:

$$P(\theta) = \begin{cases} 1 & \text{if} \begin{cases} 4.2 \leq \log(T_{\text{eff}}) \leq 4.7 \\ 0 \leq A_0 \leq 15 \\ 2.1 \leq R_V \leq 5.1 \\ 0 \leq \mu \leq 20 \end{cases} \\ 0 & \text{else} \end{cases} \quad (2)$$

[2] http://stev.oapd.inaf.it/cgi-bin/cmd
[3] This is not strictly true for μ and is a further reason to treat this parameter with caution.

Table 2. Breakdown of the number of OB candidates according to effective temperature and fit quality.

	$\chi^2 \leq 7.82$	$\chi^2 > 7.82$
O Stars: $\log(T_{\text{eff}}) \geq 4.477$	905	1090
B2–B0: $4.30 \leq \log(T_{\text{eff}}) < 4.477$	5010	1039
Late B: $\log(T_{\text{eff}}) < 4.30$	5170	1686
All $\log(T_{\text{eff}})$	11 085	3815

The lower limit on $\log(T_{\text{eff}})$ is chosen to be below the temperature of a B3V star (cf. table 3 in Nieva 2013) and the upper limit is the maximum temperature of an MS star in the Padova isochrones. The latter corresponds to earlier than O3V (see e.g. Martins, Schaerer & Hillier 2005). The upper limit on A_0 is chosen to comfortably enclose the likely extinction range among the selected OB stars, given the $g = 20$ limiting magnitude, assuming a typical rate of rise in A_0 of ~ 1.5 mag kpc^{-1}. The limits on R_V cover what we expect to find in the Galaxy (Fitzpatrick & Massa 2007) and the upper limit on μ amounts to leaving it unbound. The MCMC fitting procedure was performed using the PYTHON package EMCEE (Foreman-Mackey et al. 2013).

As in Mohr-Smith et al. (2015), SED fits with $\chi^2 < 7.82$ are taken to be acceptable: the probability of achieving this value in the case of the null hypothesis is 0.05 for the 3 degrees of freedom involved in this fitting process.

3 RESULTS OF THE PHOTOMETRIC SELECTION

3.1 Overview

Table 2 shows the breakdown of the number of OB candidates according to effective temperature and fit quality. In total, 14 900 OB stars were selected for SED fitting. Around a quarter of the candidates were found to have poor, $\chi^2 > 7.82$ SED fits. This leaves a clear majority of object with acceptable SED fits. Just under half of these are probable B3 and later type stars with $\log(T_{\text{eff}}) < 4.30$. So finally, there are 5915 objects in our target effective temperature range, $\log(T_{\text{eff}}) \geq 4.30$, with $\chi^2 < 7.82$. Of these, 905 are probable O stars with $\log(T_{\text{eff}}) \geq 4.477$. There are thus around five times as many B2–B0 star candidates as O star candidates – a ratio that exceeds the IMF ratio of ~ 3, thanks in part to the bright magnitude limit of the survey data.
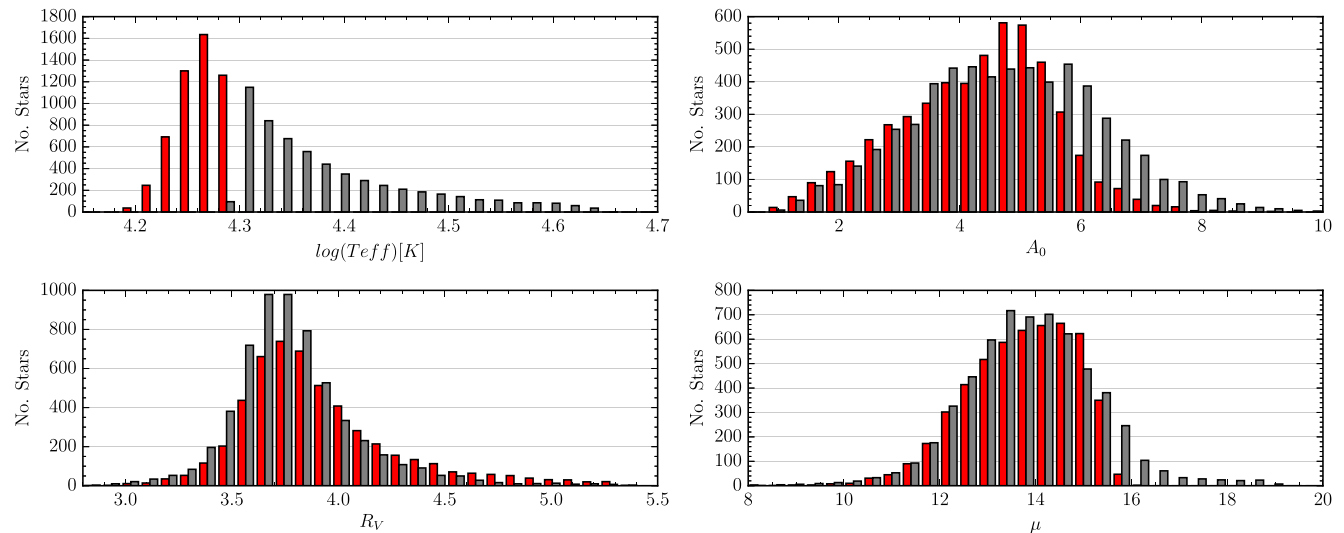
All candidates were cross-matched with SIMBAD to within an acceptance radius of 1 arcsec in order to check if any objects with already known spectral type are in the photometric selection. Table 3 shows a numerical breakdown, according to derived effective temperature and fit quality, of the subset of OB candidates with spectroscopically confirmed types according to SIMBAD. These are supplemented with the spectroscopically confirmed types from our AAOmega spectroscopy to be presented in Section 4. The majority of objects with known spectral type from SIMBAD were found to be OB stars as expected, with some WR stars appearing in the $\chi^2 > 7.82$ groupings. There is also contamination from a handful of M giant stars and one carbon star (C*) among the poor fits. These objects have mimicked very highly reddened OB stars in the $(u - g, g - r)$ diagram but nevertheless they are easily distinguished in the selection both via SED fit quality and via $r - i$ colour as discussed in Section 3.2.2. A very positive feature of Tables 2 and 3, in combination, is the high success rate in placing stars correctly into the O and B spectral types. Inevitably, the application of a cut in

Table 3. Breakdown of the number of selected OB candidates with spectroscopically confirmed types according to SIMBAD and those with spectroscopically confirmed types from AAOmega in Section 4.
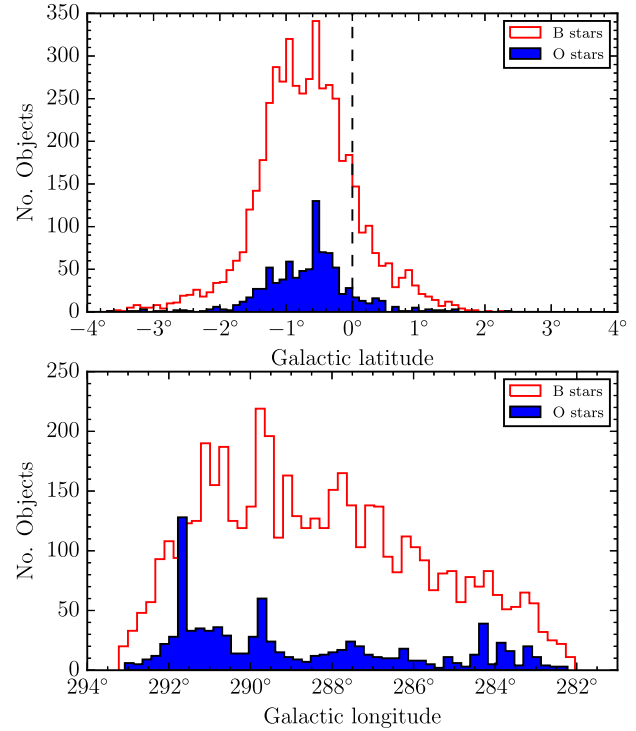
	$\chi^2 \leq 7.82$	$\chi^2 > 7.82$
$\log(T_{\rm eff}) \geq 4.477$		
AAOmega-confirmed O	18	0
Confirmed B	5	2
Other	3 A/F/G	9 A/F/G
SIMBAD-confirmed O	23	7
confirmed B	3	4
Other	2 WR	3 WR and 7M
$4.30 \leq \log(T_{\rm eff}) < 4.477$		
AAOmega-confirmed O	10	1
confirmed B	174	10
Other	6 A/F/G	2 A/F/G
SIMBAD-confirmed O	4	2
confirmed B	18	15
Other	1WR	13 WR and 1 M and 1 C*
$\log(T_{\rm eff}) < 4.30$		
AAOmega-confirmed O	0	0
confirmed B	3	2
Other	0	2 A/F/G
SIMBAD-confirmed O	0	0
confirmed B	6	1
Other	0	10 WR and 1 M

χ^2 will exclude some genuine O and early-B stars, either randomly or because of source blending and/or the presence of circumstellar emission.

Fig. 3 shows the distributions of parameters for all objects with acceptable ($\chi^2 < 7.82$) SED fits. Objects with $\log(T_{\rm eff}) \geq 4.30$ that are our main focus are coloured grey. As was found for the test case by Mohr-Smith et al. (2015), the entire region requires extinction laws with enhanced values of R_V with a median value of 3.74. The majority of the candidates have best-fitting extinctions in the range ($3 < A_0 < 6$) at likely distances of 3–10 kpc. The Galactic longitude and latitude distributions of the accepted OB stars are shown in Fig. 4. There is evidently a broad peak in the

Figure 4. The distribution in Galactic latitude and longitude of O and early-B star candidates ($\chi^2 < 7.82$). The B star distribution is in red and the O star distribution is in blue (filled). The dashed line marks $b = 0$. The strongest peaks in the O star distributions in both panels are associated with the NGC 3603 region.

latitude distribution between the Galactic equator and $b \simeq -1°.5$. The longitude distribution, on the other hand, shows a gradual rise with increasing separation from the tangent direction. The sharp O star peak in the latter, sitting close to $\ell = 292°$, is associated with NGC 3603.

The restrictions on the magnitude range of the photometry sourced from VPHAS+, in combination with photometry from
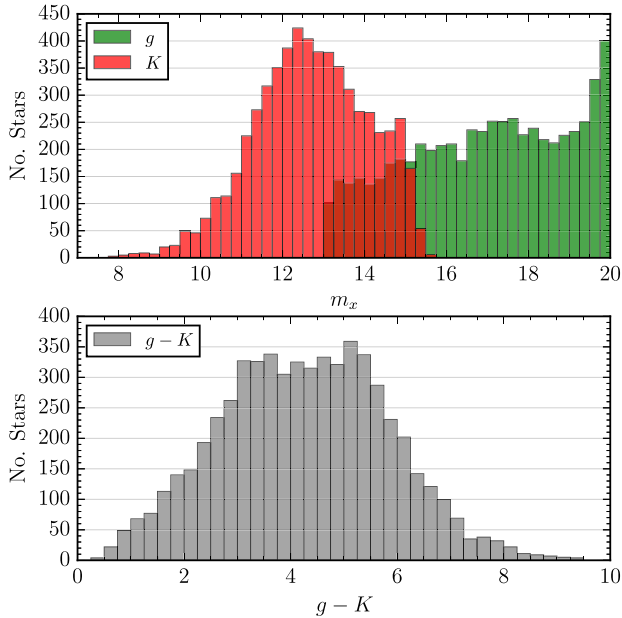

Figure 3. Distribution of the best-fitting parameters for the selection of objects with $\chi^2 < 7.82$. Objects with $\log(T_{\rm eff}) > 4.30$ are coloured in grey. The remaining cooler objects are coloured red. The turn-over in the $\log(T_{\rm eff})$ distribution at $\sim$4.26 is a product of the initial photometric selection seeking to exclude cooler B3 and later type stars.

Figure 5. Top panel: g- and K-band magnitude distribution of $\chi^2 < 7.82$ $\log(T_{\rm eff}) > 4.295$ objects. Bottom panel: $g - K$ distribution.

2MASS, inevitably carry through to some constraint on the properties of the candidates uncovered by the selection and SED fitting process. This is illustrated in Fig. 5, showing the distribution of g-band magnitudes and $g - K$ colours of all candidates with acceptable B3 or earlier type SED fits. The fact that the magnitude ranges of the VPHAS+ g and 2MASS K band only overlap within the range $13 \lesssim m \lesssim 15$ prevents us from detecting a greater number of intrinsically fainter and less-reddened hot stars with lower $g - K$. As we are targeting intrinsically bright massive OB stars, rather than sdO and sdB stars, this is not detrimental to our intended goal.

A notable feature of the g distribution is the sharp upturn in the number of candidates as the $g = 20$ faint limit is approached. This effect can be attributed to the growing number of sub-luminous objects at these faint magnitudes as discussed in detail in Section 3.2.1. At $g > 19$, we are seeing the mixing of two separate distributions; one for the massive OB stars and another for the sdO and sdB stars. If the faint g-band limit on the selection had been raised from 20th to 21st magnitude, it is likely that some more highly reddened OB stars would have been found, along with a higher proportion of sub-dwarfs. Nevertheless, the main motive behind setting the selection limit at $g = 20$ was to avoid growing incompleteness due to the increasing incidence at high extinction of u non-detections (the typical VPHAS+ 10σ faint limit is between 21 and 21.5 in g, in the Vega system).

A data base containing information on all 14 900 candidate objects is provided as supplementary material suitable for sorting by e.g. χ^2. An explanation of the data base content is set out in the Appendix. The adopted naming convention is of the form 'VPHAS_OB1_NNNNN', where 'NNNNN' is the identification number for individual objects ordered by Galactic longitude.

3.2 The identification of non-MS OB stars and emission-line objects

The SED fitting performed on our blue photometric selection could not distinguish luminosity class, nor did it make practical sense to take into consideration the possibility of line emission. So now, we use evidence from the distributions of SED-fit parameters to relax the MS assumption of the SED fits and then bring in narrow-band Hα photometry to distinguish the emission-line stars.

3.2.1 Sub- and overluminous stars

Due to the large numbers of objects included in this selection, it becomes more difficult to separate the sub-luminous and overluminous stars in the same manner as in Mohr-Smith et al. (2015). This is because the different luminosity groups drawn from a much wider sky area start to mix in the μ versus A_0 and μ versus $\log(T_{\rm eff})$ diagrams used in the selection. Here, a different technique is necessary.

We can separate sub-luminous and overluminous stars from our MS OB star targets primarily using the colour–magnitude diagram (CMD). In the $(g, u - g)$ CMD, the sub-luminous and overluminous stars will, for a given temperature and distance, form separate sequences below and above the MS. As we are looking at a range of distances, these sequences become somewhat blended. Hence, we aim to make a crude cut that errs on the conservative side.

First, we take all objects with acceptable $\chi^2 < 7.82$ fits and bin the data into deciles in effective temperature. For each decile, we then take the lowest effective temperature and the reddening vector corresponding to it and place that vector at the 95th percentile in the distance modulus (based on all temperatures in the decile) on the $(g, u - g)$ CMD. All stars fainter than this plausible lower limit line are selected as sub-luminous (see Fig. 6): they are statistically fainter than the coolest and most distant MS stars in their temperature bin. We also take the highest temperature in each bin and place it at the 5th percentile in the distance modulus on the $(g, u - g)$ CMD. All stars brighter than this line are selected as overluminous: they are statistically brighter than the hottest and closest MS stars in their temperature bin.

Fig. 6 shows the CMD, $\log(T_{\rm eff})$ versus μ and A_0 versus μ with likely MS stars in grey and the selected sub-luminous and overluminous stars in red and green, respectively. These distributions are compared with the positioning of examples confirmed as either sub- or overluminous relative to the MS assumption. In all three diagrams, the known evolved OB stars reassuringly tend to co-locate in the diagram with the overluminous candidates, whilst the one confirmed lower luminosity object also falls in the right zone.

The impact of the MS assumption in SED fits to the underluminous objects is to make them appear as very distant objects with relatively low reddening. The absolute magnitudes of sdO stars range from $M_V = 3$–6 (Stark & Wade 2003) – some ~ 6 mag fainter than MS OB stars for a given temperature. If this adjustment is made, their inferred distance moduli reduce to ~ 10–12 from ~ 16–18. Viewed in these terms, these objects would most likely be significantly reddened sub-dwarfs in the foreground of the main massive OB population. This is tenable for the less-reddened sub-luminous candidates, but especially where A_0 is 4 or more (a typical value for the MS OB stars), it becomes more likely that any downward correction of the distance modulus needs to be more modest – which, in turn, hints at classification as e.g. post-asymptotic giant branch (AGB), rather than lower mass horizontal branch. We remind there is a bias to select more highly reddened sub-dwarf stars due to the 2MASS faint limit (see Section 3.1).

Conversely, in Fig. 6, the overluminous objects appear erroneously as close-by with higher-than-average reddening. If these objects are, for example, blue supergiants (BSGs), their absolute
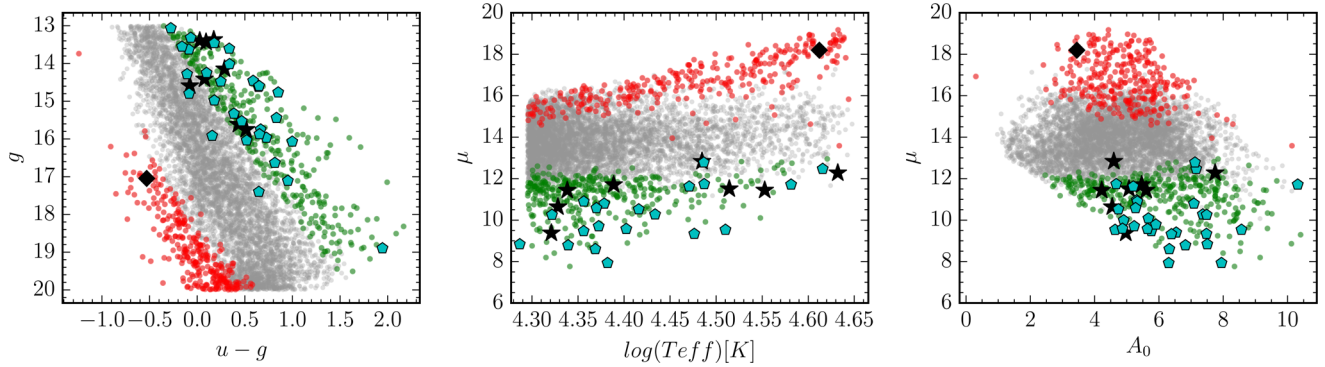
Figure 6. Objects coloured in red are likely to be sub-luminous relative to the rest of the population. Objects coloured in green are probable overluminous objects. The black diamond is the candidate sdO object with a spectrum, presented in Section 4. The cyan pentagons pick out known WR stars and the black stars represent known/confirmed luminosity class I and II OB stars.

visual magnitudes would be around ~ -6.5 (Crowther, Lennon & Walborn [2006]). If these are adopted in place of MS values, their derived distance moduli, μ, would rise from ~ 10 to ~ 14, placing them in the midst of the general near-MS massive OB population. From our own spectroscopy (Section 4) and also from the literature, we have eight objects plotted in Fig. 6 that illustrate this behaviour.

There will be some over and underluminous objects which we cannot distinguish clearly from the MS population and indeed objects falsely labelled as probably under or overluminous objects. For example, in the middle panel of Fig. 6, the distance moduli of the coolest candidate sub-dwarfs seemingly entirely overlaps the upper end of the main stellar locus. In total, 299 objects are tagged as likely to be underluminous, while 344 are tagged overluminous. This equates to around 5 per cent of the whole sample going into each category – a proportion that is a direct consequence of the distance modulus percentile cuts chosen (95th for overluminous and 5th for the sub-luminous). This cut was chosen by visual inspection of the CMD, noting where the sequences show signs of separating.

Meylan & Maeder ([1983]) estimated a surface density of 10–20 BSGs per kpc^2 in the Galactic plane. Taking our distance range as 3–10 kpc, we are sampling a projected disc surface area of a little over 9 kpc^2. This suggests that our selection of 344 overluminous stars is too generous by a factor of 2 or more. Turning to the faint end of the range, we note that Han et al. ([2003]) proposed a space density of sdB stars of 2–4×10^{-6} pc^{-3}. Assuming that we are detecting sdB stars at distances between 1 and 2.5 kpc, we are then sampling a volume of around ~ 0.06 kpc^3 which predicts around ~ 180 sdB stars. Again, this suggests a somewhat overenthusiastic selection of 344 possible sub-luminous stars. The fact that these selections 'overshoot' suggests that the remaining 90 per cent is likely to be a relatively clean selection of near MS OB stars.

The candidate stars selected as candidate over and underluminous stars are marked as such in the supplementary table (see Table A1 in the Appendix).
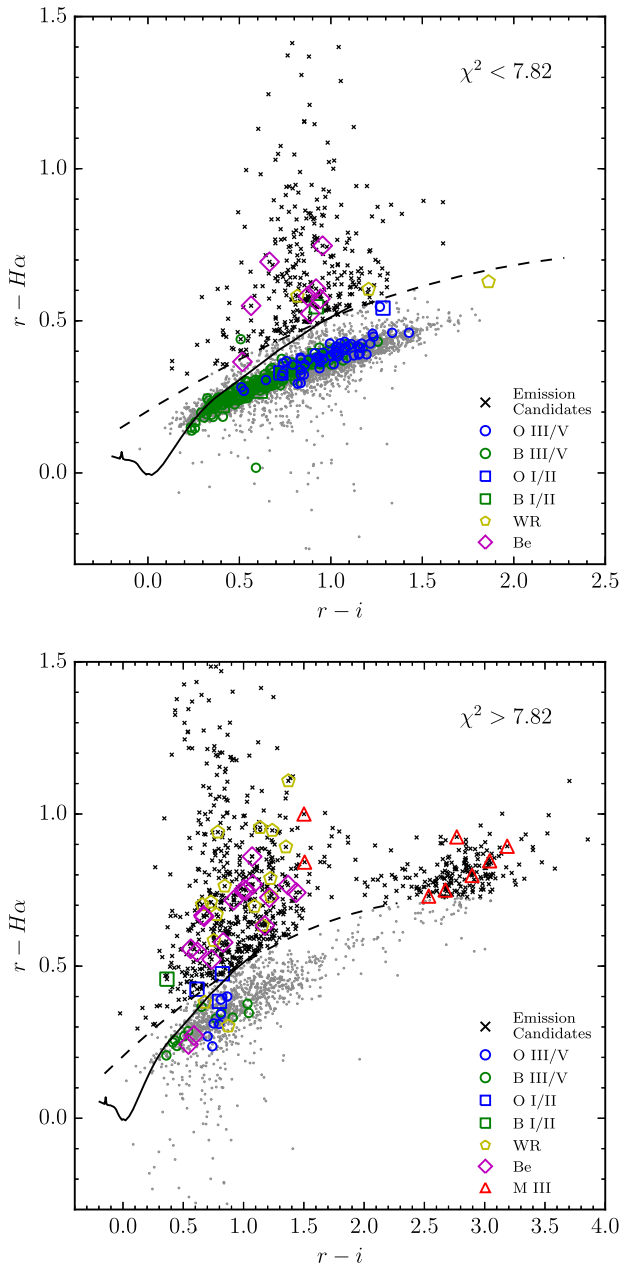
3.2.2 Emission-line stars

We now use the VPHAS+ Hα measurements to pick out any emission-line stars in our basic blue selection. Following Mohr-Smith et al. ([2015]), we use the $(r - i, r - H\alpha)$ diagram to select all objects that lie more than 0.1 mag in $r - H\alpha$ above the O9V reddening vector (equating to ~ 10 Å in emission-line equivalent

width). This secondary selection misses out 152 stars (~ 1 per cent) that are presently without recorded Hα magnitudes for quality reasons. Fig. 7 shows this selection for objects with $\log(T_{\rm eff}) \geq 4.30$ in the accepted fit group (top panel) and the poor fit group ($\chi^2 > 7.82$, bottom panel). The black crosses show objects selected as emission-line stars, while the various coloured symbols show stars with known spectral type from the SIMBAD cross-match and those with AAOmega spectra from Section 4. Here, we can see that the emission-line objects co-locate in the diagram with classical Be (CBe) stars and WR stars, while the non-emission-line objects co-locate in the diagram with the known dwarf and giant OB stars. Previous experience with the same selection method in the Northern hemisphere has shown that most candidate emission-line stars are CBe stars, at least at brighter magnitudes (Raddi et al. [2015]). As discussed in Section 4.2, the majority of WR and CBe stars produce poor χ^2 values when fit to MS OB star SEDs.

The bottom panel of Fig. 7 shows, in addition, a group of poor χ^2 objects with $r - i > 2$ that co-locate with a group of known M giant stars. These very red contaminant objects showing extreme $r - i$ values are found in the bottom right corner of the $(u - g, g - r)$ CC diagram, permitting them to enter into the original selection as candidate highly reddened OB stars. It is likely that the measured u-band magnitudes for these intrinsically red objects is affected by red leak (discussed by Drew et al. [2014]), pushing them apparently blueward into the OB-star area of the diagram. The fact that none of these objects yields a fit with $\chi^2 < 7.82$ is further illustration of how the SED fitting is critical in enhancing the overall blue-selection quality.

How the candidate emission-line stars are distributed in terms of χ^2 and broad spectral type is illustrated in Fig. 8. The growth in the fraction of emission-line candidates with declining fit quality stands out. The numbers provided in the diagram also show that it is the later B group that presents the highest fractions as well as the highest absolute numbers. Taking all the B stars together with good fits from the first two χ^2 ranges in Fig. 8, the computed fraction of emission-line stars is 7.0 per cent. This rises to 8.0 per cent, if χ^2 up to 12 is accepted also. Given that LBV and B[e] stars are rolled in, these overall fractions certainly appear consistent with the findings of McSwain & Gies ([2005]), as summarized in fig. 5 of their paper. Our estimates cannot support the 10–20 per cent range that emerged from the study by Zorec & Briot ([1997]). The differences here may well reflect the way in which CBe stars are distinguished from normal B stars. We place a clear threshold in
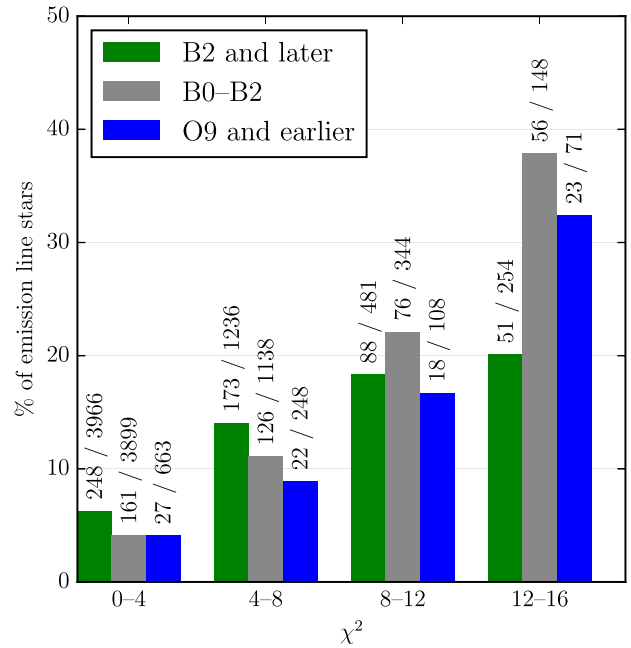
Figure 7. Emission-line stars selected using the VPHAS+ $(r - i, r - H\alpha)$ diagram with stars of known spectral class identified using coloured symbols. The top panel shows OB candidates with $\chi^2 < 7.82$ and the bottom panel shows OB candidates with $\chi^2 > 7.82$. Note the wider $r - i$ scale in the bottom panel.

requiring evidence of an Hα colour excess equivalent to at least 10 Å emission equivalent width across an observed population – an approach that is similar to that of McSwain & Gies (2005) who studied southern clusters. In older works, quantitative thresholds of this kind were less commonly applied.

Objects with Hα excess are marked as such in the data base provided in the supplementary materials. Objects with Hα emission are removed from the later discussion in Section 5 regarding extinction as the derived extinction parameters may be affected by the presence of a circumstellar disc.

Figure 8. The fraction of emission-line stars relative to the total number of objects selected in three different spectral type groups, as a function of SED fit quality (χ^2). The numbers of objects contributing to each ratio are provided above the coloured bar representing the fraction. As noted in text, the presence of circumstellar emission in an OB stellar SED unavoidably reduces the quality of fit to a pure photospheric SED. Hence, the fraction of emission-line stars rises as χ^2 rises, in all three groups, although the absolute numbers of objects fall. CBe stars and some B[e] and LBV objects most likely dominate the B spectral type range, while WR stars will be most frequent in the O range.

4 DIRECT SPECTROSCOPIC VALIDATION OF THE PHOTOMETRIC SELECTION AND SED FITS

We now present the new spectroscopy, which was already used to supplement the known SIMBAD-listed objects in Table 3, in order to appraise the quality of outcome from our photometric selection and SED fitting procedures.

4.1 Spectroscopic observations

Low-resolution spectra of 323 OB candidates ($13 < g < 19$) from our selection were taken using the multifibre spectrograph, AAOmega, at the Anglo–Australian Telescope, in service mode during 2014 June and July. The targets observed were drawn at random from across the χ^2 and effective temperature range (i.e. some poor fits were included). The large white circle in Fig. 1 shows the AAOmega 2° field of view centred on RA 10 28 45.25, Dec. −58 25 56.12 (J2000) containing all observed targets.

The 580V grating was used, covering the wavelength range ~3000–6000 Å at a resolution of $R = 1300$, in order to capture the critical blue hydrogen and helium photospheric lines needed for reliable classification. The 'red' arm grating, chosen mainly for a different programme, was the 1700D: this captured the calcium triplet region which provided some further classification evidence. We used dedicated sky fibres to support pipeline sky subtraction. The data were extracted and reduced to one-dimensional form using the 2dfdr software package with default settings; the wavelength calibration was obtained using a third-order polynomial fit. Due to

the large magnitude range of the candidates the observations were split into two configurations; a faint set-up and a bright set-up. The faint set-up included objects in the magnitude range $16 \leq g < 19$ and was exposed for a total of 140 min. The bright set-up included objects in the magnitude range $13 \leq g < 16$ and needed only 40 min exposure. Some of the spectra had to be discarded due to inadequate counts for classification purposes. The 276 spectra retained span a range in signal-to-noise ratio from 20 to 50 with a median value of 35 as measured in the wavelength range 4560–4650 Å.

Each spectrum was continuum fitted and normalized using a spline fit in the PYRAF package ONEDSPEC. Before further analysis, the prominent diffuse interstellar bands (DIBs) at $\lambda \simeq 4430, 4892, 4748$ and 5362 Å were cut out.

4.2 Broad classification of the spectra

The 'blue' and 'red' wavelength range of each stellar spectrum was visually inspected in order to place the objects into broad spectral types. Of the 276 candidates observed, using the spectral features listed below, we found that the spectral classes break down as follows:

(i) 196 B stars (He I absorption lines),
(ii) 29 O stars (He I and He II absorption),
(iii) 27 CBe stars (H β emission and He I absorption and double peaked Paschen lines),
(iv) 22 A/F/G stars (G band, calcium triplet absorption),
(v) 2 WR stars (previously known),

Including the more exotic CBe and WR stars among the desired massive star selection, we find the remaining contamination comes from just a handful of lower mass A-, F- and G-type stars. Subsequent close inspection of the original VPHAS+ data revealed that all of the A/F/G stars had photometry that was compromised either by source de-blending failures or by poor background subtraction due to a very bright neighbouring star or by falling close to the edge of a CCD (corrupting the photometry in one or more bands).

Fig. 9 shows the distribution of spectral classes for the selection. The distribution in red is for those objects that have unacceptable $\chi^2 > 7.82$ photometric SED fits. Here we can see that the majority of A/F/G star contaminants have emerged with poor fits to MS OB star SEDs thanks to the contaminated photometry. For studies focused on small numbers of objects, it is quite easy to limit contamination of the selection by visually inspecting thumbnails of every star in the sample. However, when the numbers grow, this becomes increasingly less practical and the benefit becomes less obvious given the small percentage of contaminants likely. The SED fitting procedure usefully reduces the contamination rate from 8 per cent to just 3 per cent when making a cut at $\chi^2 < 7.82$.

We also note that around 70 per cent of the CBe stars are found to have poor χ^2 values. Although the OnIR SEDs of CBe stars are not greatly different from normal B stars of similar effective temperature, the presence of a warm circumstellar disc can affect the NIR colours. It is in fact easy to separate CBe stars from the rest of the population through detection of line emission via the VPHAS+ narrow-band Hα filter (see Section 3.2.2). Both previously known WR stars have similar colours to MS OB stars below 1 μm and are hence in our selection, but they do not fit well to MS OB star OnIR SEDs, again because of NIR excess – this time due to their dense stellar winds (Faherty et al. 2014). Inspection of the SED fit residuals for spectroscopically confirmed OB stars with $\chi^2 > 7.82$ reveals that most of them have been affected by blending in the NIR photometry. At these longer wavelengths, blending will be
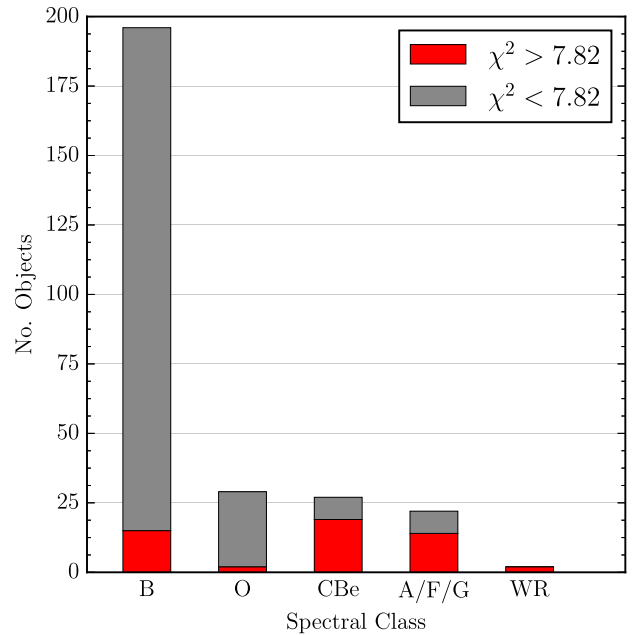
Figure 9. The distribution of broad spectral classes found for the sample of stars with AAOmega spectra.

more common due to the combination of higher prevailing stellar densities and the lower angular resolution of 2MASS.

4.3 Model atmosphere fitting

Each OB-star spectrum covering the wavelength range ~ 3000–6000 Å (225 stars in total) was fitted to a grid of model spectra in order to derive effective temperatures for comparison to our photometric estimates. The method used for the O stars had to differ from that applied to the B stars in order to adapt to different model grids, supplied in different forms. For the B stars, the TLUSTY NLTE grid (Lanz & Hubeny 2007) was used and for the O stars, the more densely sampled FASTWIND grid was fitted to these hotter objects (based on Puls et al. 2005; Simón-Díaz et al. 2011). As the full spectrum was supplied in the TLUSTY grid, the entire spectrum was used in the fitting procedure. The FASTWIND grid treats individual line profiles, including the hydrogen and helium lines needed to determine effective temperature and surface gravity – just these (stronger) lines were input to the fitting procedure. Solar metallicity was adopted in both cases. Since this sightline samples only a limited range of Galactocentric radii ($R_{\rm G} \sim 7$–10 kpc), this should be a reasonable approximation.

4.3.1 B star model fitting

We begin with a set of TLUSTY model spectra which are parametrized in terms of just effective temperate and surface gravity. Each spectrum in the grid was rotationally broadened to a range of output projected rotation velocities ($v\sin i$) and convolved to match the resolution of the instrument using the PYTHON package PYASTRONOMY. The grid was then linearly interpolated to form a continuous set of models for MCMC sampling, growing the parameter set to three:

$$\theta = \{T_{\rm eff}, \log(g), v\sin i\}. \tag{3}$$

The best-fitting parameters were derived using MCMC sampling with a χ^2 likelihood function akin to that used in the photometric fits:

$$P\left(SPEC_{\mathrm{obs}} \mid \theta\right) \propto \exp\left(-\frac{1}{2}\sum_i^n \frac{(f(obs)_i - f(mod)_i)^2}{\sigma_i^2}\right),$$
(4)

where $P(SPEC_{\mathrm{obs}}|\theta)$ is the probability of obtaining the observed spectrum ($SPEC_{\mathrm{obs}}$), given a set of parameters θ and $f(obs)_i$ and $f(mod)_i$ as the observed and model normalized flux at each wavelength i.

We compare the observed spectra to a grid of parametrized TLUSTY models using uniform priors:

$$P(\theta) = \begin{cases} 1 & \text{if} \begin{cases} 15\,\mathrm{kK} \;\leq\; T_{\mathrm{eff}} \;\leq\; 30\,\mathrm{kK} \\ 1.75 \;\leq\; \log(g) \;\leq\; 4.75 \\ 0\,\mathrm{km\,s^{-1}} \;\leq\; v\sin i \;\leq\; 600\,\mathrm{km\,s^{-1}} \end{cases} \\ 0 & \text{else} \end{cases}$$
(5)

The boundaries of the priors match the limits of the model grid.

4.3.2 O star model fitting

We deploy a set of FASTWIND models that consist of the following line profiles: H δ, H γ, H β, He I 4387, 4471, 4713, He II 4200, 4541, 4686 and 5411.

The models are parametrized by the following:

(i) T_{eff}: effective temperature,
(ii) $\log(g)$: surface gravity,
(iii) $n(\mathrm{He})$: helium abundance, by number,
(iv) ξ_t: micro turbulence,
(v) Q: wind strength parameter, $\dot{M}(Rv_\infty)^{-1.5}$,
(vi) β: exponent of the wind velocity law,
(vii) $v\sin i$: rotational velocity,
(viii) RV: heliocentric radial velocity.

In this case, each line profile was fit independently using the same style of likelihood function as equation (4). The overall function is the product of probabilities for all line profiles:

$$P(SPEC_{\mathrm{obs}} \mid \theta) \propto \prod_j^n P(LP_{\mathrm{obs}(j)} \mid \theta),$$
(6)

where $P(SPEC_{\mathrm{obs}}|\theta)$ is the probability of obtaining the observed spectrum ($SPEC_{\mathrm{obs}}$), given a set of parameters θ and where $P(LP_{\mathrm{obs}(j)}|\theta)$ is the probability of obtaining the observed line profile, $LP_{\mathrm{obs}(j)}$, again given a set of parameters θ.

The parameters ξ_t and β were fixed at typical values, $5\,\mathrm{km\,s^{-1}}$ and 0.8, respectively, as our spectra are too low resolution to detect any change in them. As for the B stars, each spectrum in the grid was rotationally broadened to deliver a set of $v\sin i$ templates, which were all subsequently convolved with a Gaussian to match the resolution of the instrument. Again, because of the limited resolution of the spectra, the contribution to line profiles from macroturbulent broadening known to affect O stars (Markova et al. 2014; Simón-Díaz & Herrero 2014) can be regarded as subsumed within the typically more prominent rotational broadening. This leaves six free parameters:

$$\theta = \{T_{\mathrm{eff}}, \log(g), v\sin i, \mathrm{RV}, \log(Q), n(\mathrm{He})\}.$$
(7)

The uniform grid of templates was linearly interpolated to form a continuous grid for MCMC sampling. The following uniform priors

for each parameter were adopted and are defined by the limits of the model grid:

$$P(\theta) = \begin{cases} 1 & \text{if} \begin{cases} 25\,\mathrm{kK} \;\leq\; T_{\mathrm{eff}} \;\leq\; 55\,\mathrm{kK} \\ 3.0 \;\leq\; \log(g) \;\leq\; 4.4 \\ 0\,\mathrm{km\,s^{-1}} \;\leq\; v\sin i \;\leq\; 600\,\mathrm{km\,s^{-1}} \\ -400\,\mathrm{km\,s^{-1}} \;\leq\; \mathrm{RV} \;\leq\; 400\,\mathrm{km\,s^{-1}}. \\ -14 \;\leq\; \log(Q) \;\leq\; -12.5 \\ 0.06 \;\leq\; n(\mathrm{He}) \;\leq\; 0.20 \end{cases} \\ 0 & \text{else} \end{cases}$$
(8)

The key constraint expected from these fits is on effective temperature. There is also useful information contained in the derived surface gravities and rotational velocities. Given the low-resolution of the spectra, we treat all the other parameters as 'nuisance parameters' since the derived values will carry large uncertainties and are not relevant to this discussion. However, their influence on the other parameters is, by default, taken into account when using the marginalized posterior probability distributions. We also tried fitting the O stars to O star NLTE TLUSTY models (Lanz & Hubeny 2003) using the same method as for the B stars and found little difference in the average derived temperatures and surface gravities compared with the FASTWIND results: we note there is a tendency for the TLUSTY models to offer combinations of slightly higher surface gravities and effective temperatures relative to FASTWIND, especially in the hottest cases (see the example discussed in the next section).

4.4 Results of the spectroscopic fitting

The median of the posterior probability distributions for each parameter is taken as the best-fitting value. The 16th and 84th percentiles are taken as the upper and lower uncertainty on each parameter. The best-fitting spectroscopic parameters for all the OB stars observed with AAOmega are added to the data base provided as supplementary material. Fig. 10 shows example spectra, after normalization and excision of DIBs present, overplotted on the best-fitting model. The top panel presents an O star spectrum compared with FASTWIND best-fitting line profiles, while the bottom panel presents a comparison between an observed B-star spectrum with an NLTE TLUSTY fit.

Fig. 11 shows the distribution in T_{eff}, $\log(g)$ and $v\sin i$ for the spectroscopic fits of OB stars. The distribution in T_{eff} peaks at around 20 kK and falls off at higher temperatures. This is very similar to the distribution in the photometric temperature estimates shown in Mohr-Smith et al. (2015). As expected, the majority of stars show MS surface gravities with a median value a little less than 4 (more precisely, 3.92). The three lowest surface gravity objects $\log(g) \lesssim 3.2$ are likely to be evolved B stars. Their relatively cool temperatures ($19\,\mathrm{kK} < T_{\mathrm{eff}} < 24\,\mathrm{kK}$) and lower surface gravities would be consistent with luminosity class II–III giants (Schmidt-Kaler 1982). Their overluminous position in the $(g, u-g)$ CMD also supports the notion that these are evolved objects (see Section 3.2.1: these are three of the objects emphasized in black in Fig. 6).

One very hot O star whose spectrum has been compared with model atmospheres has also been selected as a sub-dwarf (ID 1558) using the technique outlined in Section 3.2.1. We found that the fits both to the FASTWIND grid and to the TLUSTY (OSTAR) grid struggled with the upper limits on $\log g$ (respectively, 4.3 and 4.75: the fits returned gave $\log g = 4.2$ and 4.7). To overcome this problem, we carried out a fit against a grid of hydrogen and helium NLTE
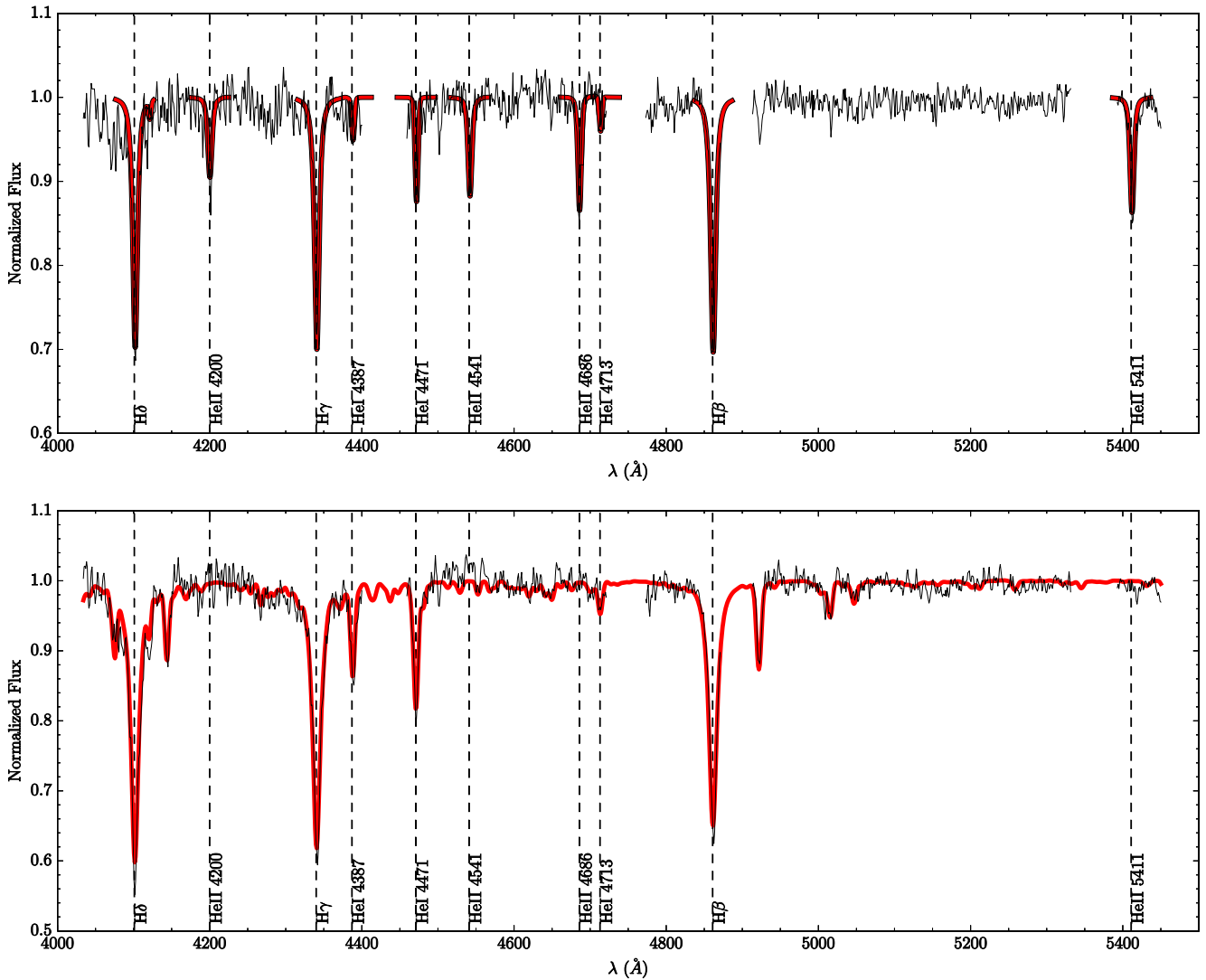
Figure 10. Example of spectra and best-fitting models. Top: ID #1374, $g = 15.5$ mag, $A_0 = 5.6$, $T_{eff} = 38\,600$ K and $\log(g) = 4.19$, with the FASTWIND fit to the hydrogen and helium lines superimposed in red. Bottom: ID #2593 $g = 17.2$ mag, $A_0 = 4.5$, $T_{eff} = 23\,100$ K and $\log(g) = 4.32$, with the TLUSTY NLTE full spectrum fit superimposed. The signal-to-noise ratios of the two spectra are $\sim$25 (top) and $\sim$31 (bottom).

model atmospheres used by Napiwotzki (1999) for the analysis of central stars of planetary nebulae (CSPN). The fit results are $T_{eff} = 55 \pm 2$ kK, $\log g = 4.4 \pm 0.2$ and $n(\mathrm{He}) = 0.23 \pm 0.05$. Whilst the neglect of metals in this third model grid might cause a modest systematic shift, a gravity well below what is typical for most hot sdO stars ($5.5 \lesssim \log g \lesssim 6.0$; Green et al. 2008) is supported. This and the presence of weak, spatially unresolved [O III] $\lambda\lambda$4959, 5007 in emission in this object's spectrum suggests post-AGB status for this star. Interestingly, in addition, the sdO atmosphere exhibits helium enrichment $n(\mathrm{He}) = 0.23$ and 0.15, respectively, from the CSPN and FASTWIND grids. The history of this object could be similar to that of the unusual PN central star, K648 in M15 (Rauch, Heber & Werner 2002), which shows signs of material being mixed into the atmosphere during a final helium flash. For now, we acknowledge that our one 'sub-luminous' spectroscopic target is potentially not so sub-luminous and that higher quality data are required to conclude on its nature. Nevertheless, the placement of this star in the non-massive 'sub-luminous' group is sound.

The distribution in projected rotational velocities ($v\sin i$) for the entire sample of OB stars is broadly consistent with the distributions

presented by Huang, Gies & McSwain (2010) for B stars, and by Simón-Díaz & Herrero (2014) describing O stars in the Milky Way. The values returned for this parameter are provided in the data base for individual objects for completeness. But we caution that as individual measures, they will be appreciably more uncertain than the quoted MCMC-derived random errors might suggest. This is due to limited spectral resolution (corresponding to a velocity resolution of $\sim$230 km s^{-1}) and the moderate S/N of the data (most often, 30–40) – which have both a direct impact through e.g. uncertainties in continuum placement and more indirectly through the lack of capacity to distinguish binarity (SB2 component blending).

4.5 Comparison of the spectroscopic and photometric best-fitting effective temperatures

Fig. 12 shows the effective temperatures determined from the photometric SED fits compared to those determined by spectroscopy. The red circles show objects with $\chi^2 > 7.82$ in the SED fitting routine. We find that, despite the necessary reservations about determining effective temperatures through photometry alone, there
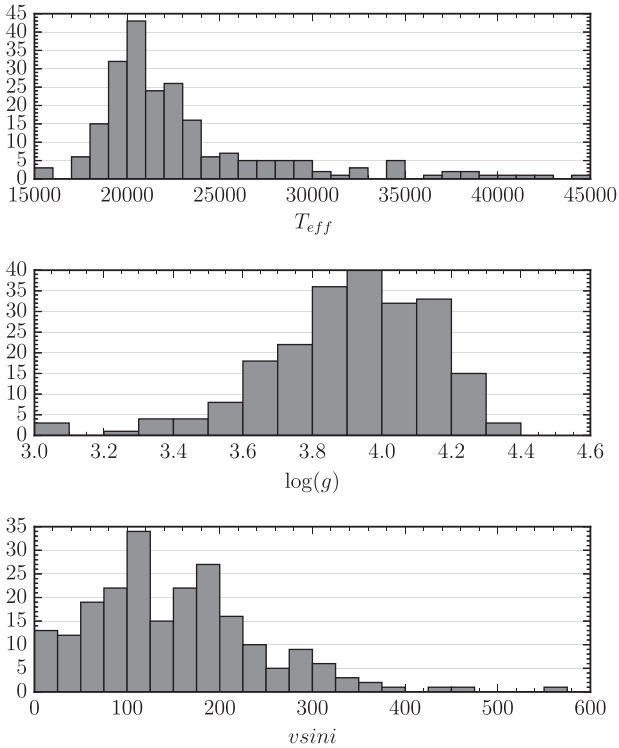
Figure 11. The distributions of effective temperature, surface gravity and projected rotational velocity obtained from the spectroscopic fits.
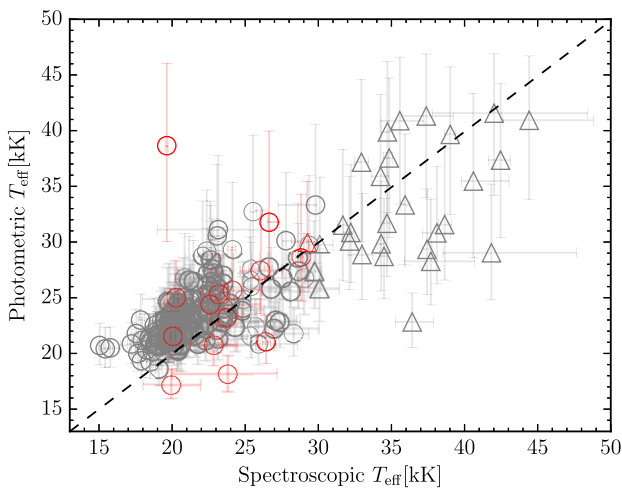
Figure 12. Comparison of the derived effective temperature from the photometric SED fitting with those derived from spectroscopy. The triangles are O stars and the circles are B stars. Symbols coloured in red correspond to stars whose photometric SED fits gave $\chi^2 > 7.82$.

is a good correlation between the two methods. We do however see a systematic tendency in the photometric method to underestimate the temperature of O stars and overestimate those of the B stars, when compared to the spectroscopy. As the photometric calibration appears to be well behaved, this is most likely to be due to differences between the photometric effective temperature scales in the Padova isochrones (based on local thermodynamic equilibrium model atmospheres; Bressan et al. 2012) and those relevant to the TLUSTY and FASTWIND NLTE models used to fit the spectra. Another factor that affects the extreme cases is photometric blending or contamination. For example, the poor χ^2 object with the largest

disagreement is close to a very red object which is very likely to have affected the measured magnitudes, particularly 2MASS *J* to *K*.

With the extra information on temperature provided by the spectroscopic fits, we can check what effect the systematic offset in the photometrically derived $\log(T_{\rm eff})$ has on the derived reddening parameters. To do this, we recalculated the SED fits using a much narrower uniform prior on temperature, based on the 16th and 84th percentiles of the marginalized posterior distribution of spectroscopic temperature for each star (as indicated by the horizontal error bars in Figs 12 and 13). Fig. 13 shows the impact on the derived values of A_0 and R_V when the more precise 'restricted' temperature prior is used in place of almost no constraint in the SED fitting. Here we can see that for both reddening parameters that restricting $\log(T_{\rm eff})$ has a greater effect on stars below ~25 kK. This is due to the higher sensitivity of the shape of the SED as a function of temperature for the cooler stars. At effective temperatures above ~25 kK, the SEDs approach the Rayleigh–Jeans limit more closely, lowering the sensitivity to temperature: in this regime, the shape of the SED is almost entirely dominated by extinction.

It is important to notice that these systematic effects are very small; for stars with $T_{\rm eff} \geq 25$ kK, the median difference in A_0 and R_V ('free' – 'restricted') is, respectively, −0.025 and 0.026, and for those with $T_{\rm eff} < 25$ kK, the median differences rise to 0.09 and −0.07. In the worst cases, these systematic uncertainties are comparable to the random uncertainties on the parameters due to the photometric errors. However, whilst there is indeed a modest disagreement between the photometric and spectroscopic effective temperature scales, it would amount to forcing photometric fits to systematically 'incorrect' SED models if the temperature prior were restricted to suit the spectroscopic results. This idea is supported by systematically poorer fits in the 'restricted' case where the median $\chi^2 = 2.99$, in contrast to $\chi^2 = 1.58$ in the 'free' case. Accordingly, it does not make sense to regard the trends seen in Fig. 13 as providing a systematic correction to the parameter estimates based on photometry. What it does all point to is the issue of fit degeneracy between effective temperature and extinction: this begins to acquire some significance towards the cool end of the OB range where we find the larger discrepancies. But the magnitude of this effect is very much smaller than that affecting fits to broad-band photometry of A- to K-type stars (see Bailer-Jones 2011), underlining the long-recognized value of OB stars in tracing Galactic extinction.

5 EXTINCTION PROPERTIES AND SPATIAL DISTRIBUTION

It was demonstrated by Mohr-Smith et al. (2015) and also in preceding sections that the SED-fitting process places strongest constraints on the reddening parameters, A_0 and R_V, achieving typical precisions in the region of ±0.1. These are now put to use to better understand the full pencil beam, passing through the Carina Arm to distances at least as great as ~7 kpc, the distance to NGC 3603. We begin with an overview of extinction across the region, before extracting more detail.

In this analysis and discussion, we remove from consideration the objects tagged as either emission-line stars or as potentially sub-luminous (reducing 5915 objects to 4770).

5.1 Overview of extinction in the region

It is already well known, going back in the literature to before Cardelli et al. (1989), that the Carina region is associated with flatter
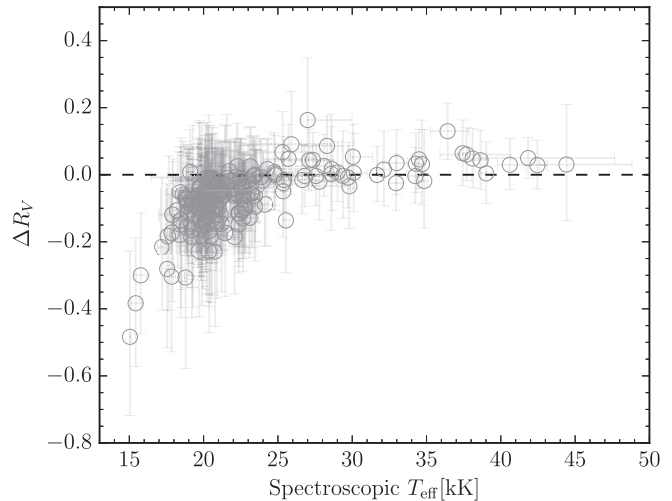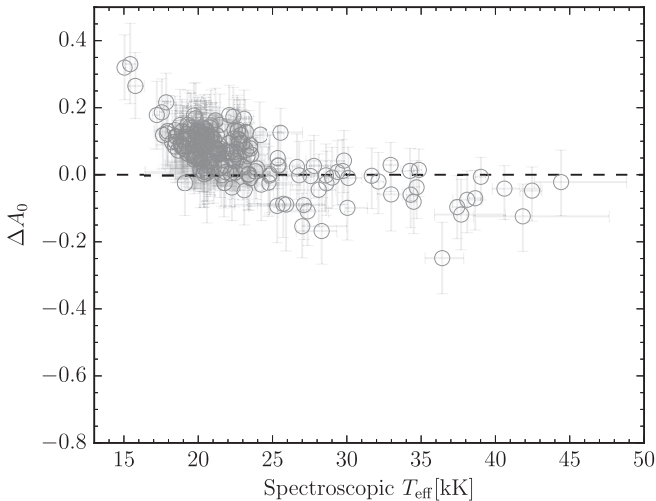
Figure 13. Change in derived reddening parameters when using a temperature prior defined by the spectroscopic fits. The difference (free – fixed) is shown on the vertical axis.

extinction laws, characterized by higher R_V (>3.5). Fitzpatrick & Massa (2007) and Hur et al. (2012) found this near the open clusters Trumpler 16 (Tr 16) and NGC 3293, whilst normal values of $R_V \sim$ 3.1 still seem to apply to less-reddened stars with $A_0 \lesssim 2$ mag. In the *Chandra* X-ray study of the wider Carina Nebula, spanning a sky area of 1.49 $\deg^2$, Povich et al. (2011) confirmed this general pattern and recommended $R_V = 4$ as representative of higher extinctions (from $A_V \simeq 1.8$ to 4, based on an X-ray selected sample of 94 OB candidates).

First, we need to identify the spatial and extinction parameter domain open to examination. To this end, we consider the constraints set by the sample magnitude limits using some straightforward modelling: we take all of the photometric OB MS star models in the grid used in SED fitting ($\log (T_{\rm eff}) \geq 4.30$) and redden them, assuming a rise in A_0 of 0.8 mag kpc^{-1} (retrospectively a plausible growth rate for the region, see Section 5.3) for all values of R_V. This permits us to see which combinations of A_0 and R_V produce an SED falling within the survey-imposed limits: $12 < u < 21$, $12 < i < 21$, $12 < r < 21$ and $13 < g < 20$. We collect the fraction of simulated SEDs meeting requirement for each combination of A_0 and R_V and (by implication of the adopted A_0 rise rate) distance. This model of detectability does not reveal how many stars we expect to find in the selection given A_0 and R_V, as this would require taking into account IMF weighting, the growth in the volume captured with increasing distance and a Galactic stellar density model. Instead, our present purpose is restricted to establishing limits on the detectable (R_V, A_0) parameter space.

Fig. 14 answers this question: it turns out that the amount of extinction, A_0, places the stronger constraints, in that the detectability at $A_0 < 2$ and $A_0 > 10$ of OB stars is low. Note that only B stars are intrinsically faint enough at the low end of this range to be picked up, while only O stars are luminous enough at the other. The constraints on R_V within the open A_0 window are much weaker: there is little/no constraint on R_V until, at $A_0 > 9$, SEDs presenting $R_V \lesssim$ 2.5 become increasingly difficult to capture. This reflects the link between falling R_V and a steepening extinction law (at higher A_0), such that the u magnitude will be more readily pushed beyond the faint limit as R_V drops.

The observed distribution in R_V as a function of A_0, superimposed in Fig. 14, reveals a striking absence of correlation between these parameters, except that only below $A_0 \simeq 2$ is $R_V < 3.5$ rel-
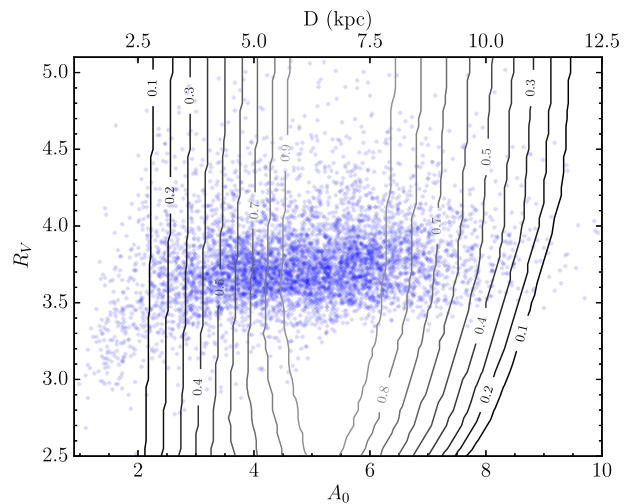
Figure 14. Contour lines estimating the OB star detection fraction in VPHAS+ for different combinations of A_0 and R_V superposed on the obtained distribution (shown in blue). An increase in extinction of 0.8 mag kpc^{-1} is adopted in the modelling of the contours – the implied heliocentric distance scale is marked across the top. The offset between the range of maximum detectability and the measured extinctions is to be expected without the incorporation of a Galactic model and IMF weighting: the drop-off in detections beyond $A_0 \sim 7$ is attributable to the overall downward trend in stellar density. The pencil beam studied exits the Solar Circle at a distance of ~ 6 kpc, while at a distance of 10 kpc, the Galactocentric radius is 10–11 kpc.

atively common. From $A_0 \gtrsim 3$ to $A_0 \sim 8$, where the distribution begins to peter out, the trend is flat and broad. Relatively few objects are picked up at distances below 2.5–3 kpc, indicating that this new sample misses out the foreground to the Carina Arm. The apparent offset between the peak detectability range defined by the contours in the figure ($4 \lesssim A_0 \lesssim 10$) and main concentration of the measurements ($3 \lesssim A_0 \lesssim 7$) has two different origins dependent on Galactic longitude: near the Carina Arm tangent, 0.8 mag kpc^{-1} is too low a growth rate in extinction, while at greater longitudes where this rate is better matched, there is a strong decline in stellar density beyond both the Solar Circle (crossed at a heliocentric distance of 5.5 kpc) and the outer Carina Arm (crossed at 7–10 kpc,
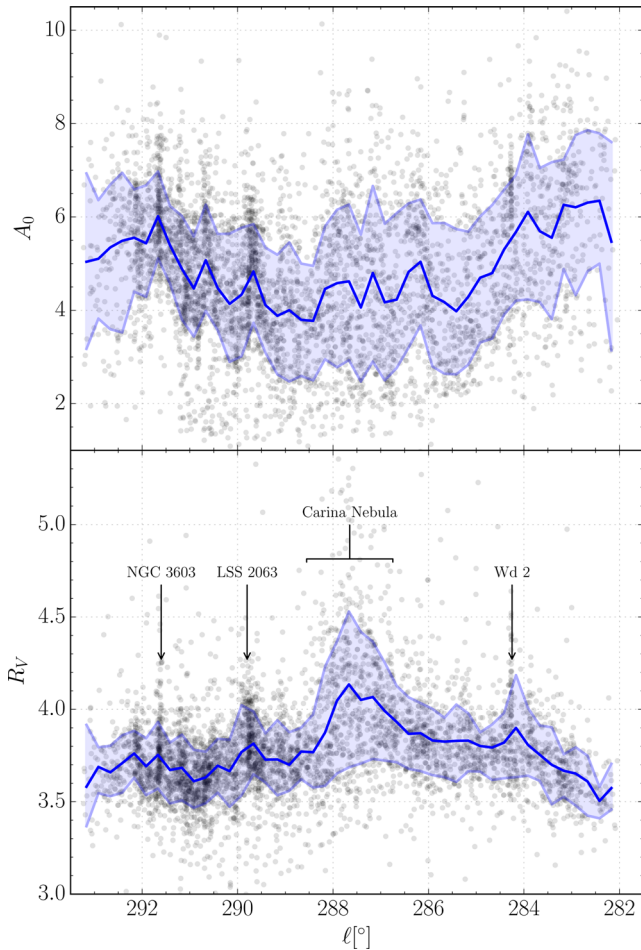
Figure 15. The distributions of A_0, top panel, and R_V, lower panel, as functions of Galactic longitude. The plot is restricted to non-emission $\chi^2 < 7.82$ candidate OB stars in the Galactic latitude range $0°0 > b > −1°5$ (4770 stars). The blue line, in both panels, is the running mean of the distribution sampled every $0°25$. The standard deviation about the mean is also shown shaded in light blue. The typical random error on each data point is ~ 0.1 (magnitudes in the case of A_0).

depending in detail on longitude). We now turn to considering the pattern of extinction variation on the plane of the sky to explain why this is so.

Fig. 15 shows how A_0 and R_V vary across the region as a function of Galactic longitude. The 4770 stars plotted are limited to the latitude range $−1°5 < b < 0°0$, the most completely and densely sampled part of the region (see Fig. 4). In the upper panel, it is unsurprising to see the wide spread in A_0 at all longitudes, but there is nevertheless the appearance of a broad dip such that the median extinction is 4–5 in the range $285° < \ell < 289°$, as compared with 5–6 to either side. This broad minimum is where the relatively nearby Carina Nebula is located.

At the lower longitudes closest to the tangent region, the A_0 distribution is most disorderly and the highest measures are found. The Planck XI dust map (Planck Collaboration XI 2014) indicates that the total dust optical depth at these longitudes is strongly variable and typically approximately twice as high as at $\ell > 285°$, implying total visual extinctions of around 15–20 mag. This is consistent with what is known of the CO distribution (Grabelsky et al. 1987). In contrast, at $\ell > 289°$, the pattern is at its most regular: indeed, there are signs of a gradual rise in extinction with increasing longitude,

passing through the location of NGC 3603. As shall become evident in Section 5.3, this trend translates into a broadly regular increase in distance sampled with increasing A_0. The OB stars found in this region mainly belong to the outer Carina Arm and more nearly sample the total dust column ($\tau_{353} \sim 2 \times 10^{-4}$ corresponding to a maximum visual extinction of 8–10; see Planck Collaboration XI 2014).

5.2 Variations in A_0 and R_V near massive clusters, and a newly identified OB association

The most striking feature in the R_V variation with Galactic longitude (lower panel in Fig. 15) is the explosion of high values in the mid-longitude range (286.5–288, roughly) occupied by the Carina Nebula: any value from ~ 3.5 up to more than 5 is apparently possible. Elsewhere, excursions beyond ~ 4 are relatively infrequent. Interestingly, echoes of this behaviour are also apparent at the longitudes of Westerlund 2 and NGC 3603. The relatively sharp spikes associated with these two clusters follow from their greater distances and correspondingly reduced angular sizes. Indeed, this result suggests that systematically higher R_V and flatter optical extinction laws – implying larger typical dust grain sizes – is a persistent property of the environments around young massive (O star-rich) clusters. This may betray greater columns of dust grain populations biased to larger typical grain sizes in the surrounding molecular gas, unused in the star formation event, or the origin may be more dynamic and arise as a consequence of star formation feedback (see e.g. Draine 2011; Allen et al. 2014; Ochsendorf & Tielens 2015): further detailed investigation is needed.

In general terms, $3.5 < R_V < 3.8$ appears typical of the Carina Arm field, while near the prominent clusters, average values of $3.7 < R_V < 4.2$ are much more frequently encountered – with the Carina Nebula presenting as an extreme case.

On collapsing the Galactic latitude distribution, as in Fig. 15 (and also in the lower panel of Fig. 4), it becomes easy to pick out the well-known massive clusters – showing up as dense concentrations, linking to localized peaks in R_V and A_0. In addition, the eye is drawn in both figures to an OB clustering near $\ell \sim 290°$ that has no clear literature counterpart, so far. A close-up of the on-sky distribution of the $\chi^2 < 7.82$ objects in this region, pinpointing the main clustering at $\ell = 289°77$, $b = −1°22$, is provided as Fig. 16, with *WISE* 8 μm (warm dust) emission added as the background. Visual extinctions 4.5–5 mag are typical. The total number of objects falling in the red box, of rough dimension 9×10 arcmin^2, superimposed on Fig. 16 is 103, of which 32 are candidate O stars.

The most dense sub-clustering of 42 objects spread across ~ 2 arcmin (coloured cyan in Fig. 16) coincides with LSS 2063, an 11th magnitude star, classified by Walborn & Fitzpatrick (2000) as O5If+. These same authors give $B − V = 1$, which we interpret as a likely visual extinction of about 5 (adopting an intrinsic colour of $−0.28$ from Martins & Plez 2006 and $R_V \sim 3.8$, on the basis of Fig. 15). This fits in well with the newly revealed clustering. In the first edition of their Galactic O-star catalogue, Maíz-Apellániz et al. (2004) cautiously described LSS 2063 as a 'field' object, there being no clear reports of an associated cluster at the time. Nevertheless, Dutra et al. (2003) did catalogue an NIR cluster essentially coincident with LSS 2063 and, more recently, Majaess (2013) has noted this location as a plausible clustering of young stars based on raised mid-IR emission (Majaess 133, in the associated catalogue). Georgelin et al. (2000) noted the H II emission here, in Gum 35 (also known as RWC 54a), and cited the Caswell & Haynes (1987) H I recombination line
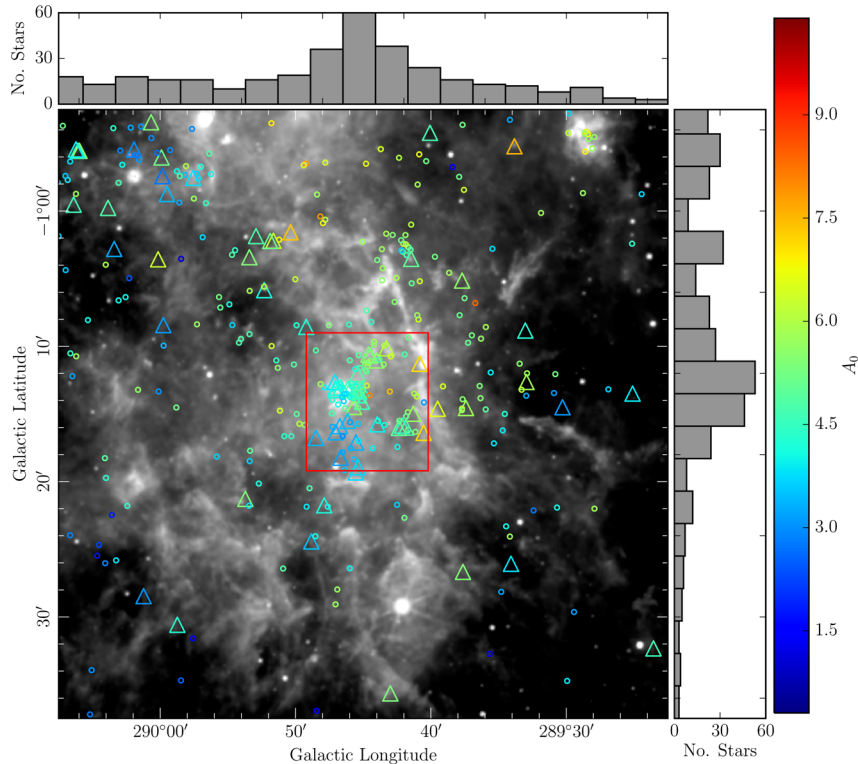
Figure 16. A hitherto unrecognized massive OB clustering, scattered around $\ell = 289°.77$, $b = -1°.22$, the position of the extreme O supergiant, LSS 2063. High-confidence OB candidates are overplotted on warm dust emission imaged at 12 μm by the *WISE* mission (Wright et al. 2010). The histograms above and to the right of the image show the Galactic longitude and latitude distributions of the objects found. Triangles indicate candidate O stars, while the smaller circles mark candidate early-B stars. Each object is coloured according to best-fitting A_0. The main concentration of 140 candidates is enclosed in a red box of dimension 0.15×0.17 deg^2.

measurement that places the region at the same kinematic distance as NGC 3603 (∼7 kpc away). Avedisova (2002), in her list of star-forming regions, also notes a coincidence between radio emission in this location and RAFGL 4120 (an earlier mid-IR detection effectively). So here, finally, the optical has caught up and the very much larger group of ionizing stars, helping LSS 2063 shape this environment, has emerged.

At a distance of about 7 kpc, the overdensity's full angular extent of 9–10 arcmin corresponds to a linear size of ∼20 pc, allowing this clustering to be viewed as an OB association. The count of 103 OB stars misses LSS 2063 itself and 4 more that are also above the VPHAS + bright limit [an O9.5 Iab star classified by Sota et al 2014 and three candidate O stars from Wramdemark (1976)]. If the 108 stars found conform to a Kroupa (2001) IMF and an MS mass of 7 M$_\odot$ may be associated with an effective temperature of 20 000 K, the implied mass of stars in the association is at least ∼8×10^3 M$_\odot$. On the same basis, the predicted number of O stars (>15 M$_\odot$) is 39 – to be compared with our estimate of 37.

5.3 The changing on-sky OB star distribution with increasing extinction

Fig. 17 shows the selected and accepted OB star candidates divided up between three different extinction windows ($A_0 \leq 4$, $4 < A_0 < 6$ and $A_0 \geq 6$). What stands out the most in this figure is that the distribution in Galactic latitude narrows as A_0 increases, revealing the receding Galactic thin disc. To express this more precisely, the on-sky angular projection of the scaleheight of the OB stars exhibits clear shrinkage with increasing reddening – hinting that reddening is statistically correlated with distance. We can use this

effect to estimate the approximate distance ranges we are sampling as a function of rising extinction. This method turns out to be more informative than relying on the distance moduli derived from the SED fits, in which the strong correlation between μ and effective temperature leads to considerable imprecision. Panel (a) of Fig. 18 shows that the trend in A_0 versus distance, D (from μ) eventually loses credibility as distance would seem to decrease with extinction beyond $A_0 = 5$. In view of this, we explore the use of the angular spread of the candidates as a proxy for distance. This depends on the finding that the OB star scaleheight in the Galactic disc appears to be broadly independent of Galactocentric radius (Paladini, Davies & De Zotti 2004).

We bin the objects in extinction from 2.5 – 8.5 in steps of $\Delta A_0 = 1$, anticipating that the OB stellar density, expressed as a function of Galactic latitude in each extinction slice, conforms to an isothermal population characterized by a single angular scaleheight $h_b = h_{OB}/D$. We adopt $h_{OB} = 45 \pm 5$ pc (Reed 2000; Bobylev & Bajkova 2016) and D is to be regarded as the representative, if fuzzy, heliocentric distance to the reddening slice. The scaleheight of OB stars, h_{OB}, is conventionally defined with reference to either a back-to-back exponential or to the square of a hyperbolic secant. For our fitting exercise, we prefer the latter for mathematical convenience. In this, we follow Conti & Vacca (1990). Specifically, we apply to each reddening slice a fit of the form:

$$N(b) = A \operatorname{sech}^2\left(\frac{b - b_0}{\sqrt{2}h_b}\right), \qquad (9)$$

in which A is a constant, proportional to the sample size, and b_0 is the Galactic latitude at which the best-fitting function peaks. With h_b the angular scaleheight, this makes three fit parameters.
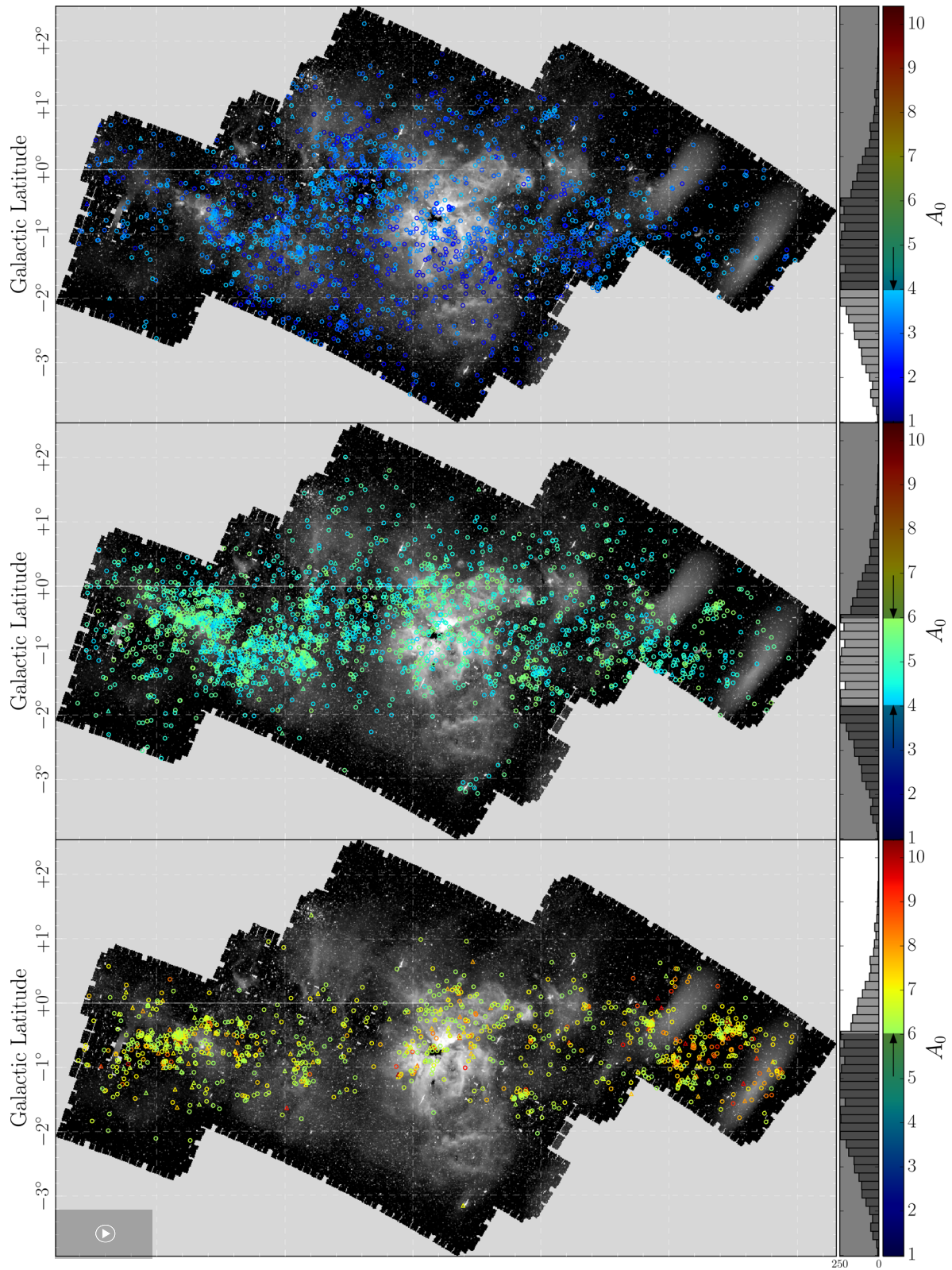
Figure 17. Three plots showing the positions of OB stars through windows increasing in A_0 (from top to bottom). O stars and early-B stars are represented as triangles and circles, respectively. The histogram to the right of each on-sky map shows the full distribution in A_0, highlighting the range mapped to the left. The online version of this figure is animated, showing the changing OB star distribution as the A_0 range shown rises.
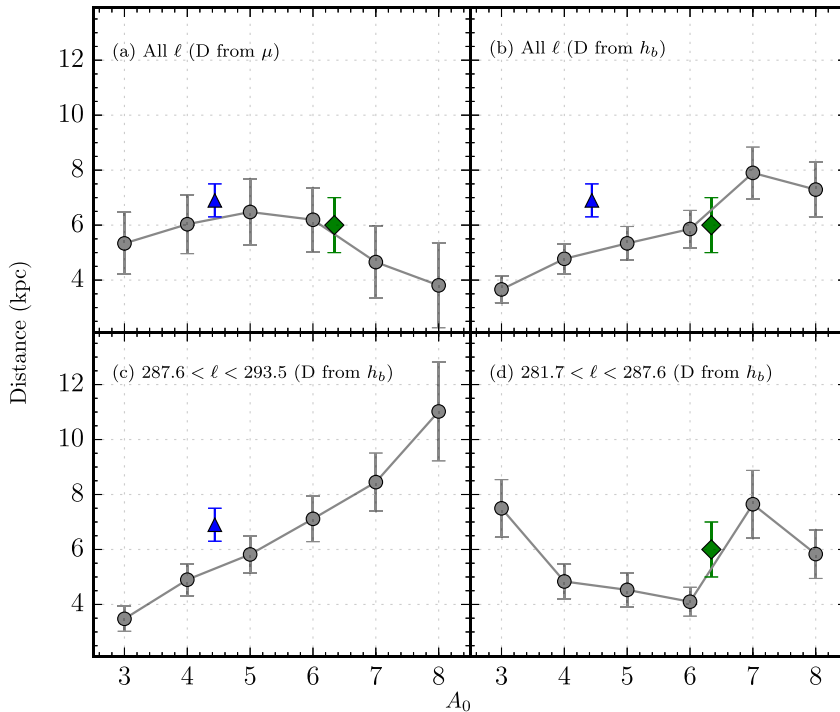
Figure 18. Panel (a): the mean distance and standard deviation obtained from the best-fitting distance modulus μ as a function of best-fitting A_0. Panel (b): here the distance is inferred as a function of A_0 based on the measured angular scaleheight (h_b) of the newly uncovered OB star population, as described in the text. This gives a much more orderly trend. The blue triangle places NGC 3603 on the diagram according to the literature consensus on its reddening and distance, while the green diamond does the same for Westerlund 2. Panels (c) and (d) are the same as (b) except that the longitude range has been split in half, with 3432 stars in the higher longitude (NGC 3603), half of the studied range in (c) and 1923 stars in the lower longitude range including Westerlund 2.

Table 4. Data and results for the fits to extinction slices constructed from the cleaned OB star sample at Galactic longitudes >287°.6, using the functional form given in equation (9). Here b_m, in the penultimate column, is the true Galactic latitude of the geometrically flat mid-plane, according to Goodman et al. (2014). In the last column, $Z_0(OB)$ is the offset in parsec of the OB-star mid-plane from flat – the estimated warp in other words.

A_0(mag)	N	$b_0(°)$	$h_b(°)$	D (kpc)	$b_m(°)$	Z_0 (OB) (pc)
2.5–3.5	477	-0.60 ± 0.06	0.75 ± 0.05	3.5 ± 0.5	-0.38	-13 ± -11
3.5–4.5	869	-0.66 ± 0.03	0.53 ± 0.02	4.9 ± 0.6	-0.26	-35 ± -5
4.5–5.5	845	-0.66 ± 0.02	0.44 ± 0.01	5.8 ± 0.7	-0.21	-46 ± -6
5.5–6.5	687	-0.65 ± 0.02	0.36 ± 0.01	7.1 ± 0.8	-0.17	-60 ± -8
6.5–7.5	233	-0.63 ± 0.03	0.30 ± 0.02	8.5 ± 1.1	-0.14	-72 ± -11
7.5–8.5	71	-0.66 ± 0.04	0.23 ± 0.03	11.0 ± 1.8	-0.10	-108 ± -23

Panels (b)–(d) of Fig. 18 show the derived distances, D, per reddening slice, for three different Galactic longitude ranges. Panel (b) shows the entire longitude range of the studied area, while panels (c) and (d) split the longitude range into two halves. Panel (c), where $287.6 < \ell < 293.2$, includes the part of the footprint that contains the cluster NGC 3603, while panel (d), where $282.0 < \ell < 287.6$, takes in the rest of the foot print containing Wd 2. For later use, we set out the numerical results of panel (c) as Table 4. The relevant panels in Fig. 18 include the distance and extinction to NGC 3603 (blue triangle) taken from Sung & Bessell (2004) and the distance and extinction to Wd 2 (green diamond) taken from Dame (2007) and Mohr-Smith et al. (2015), respectively.

Panel (c) shows that for $287.6 < l < 293.2$, we have a well-behaved steady increase in estimated distance as a function of extinction of 0.8 mag kpc^{-1}. This is the range within which the dependence of A_0 on Galactic longitude is also more organized, tending to rise as longitude increases (see Fig. 15). The literature values of extinction and distance of NGC 3603 fit as expected into

this trend, confirming that it is located in a relative reddening hole (see e.g. Pang, Pasquali & Grebel 2011).

However, for $282.0 < l < 287.6$ shown in panel (d), there is no orderly correlation between extinction and inferred distance. This difference can be attributed to the fact that for the lower longitude sight lines, the Carina Arm tangent ($l \simeq 281$; see e.g. Dame 2007) is not far away, permitting a more rapid and chaotic accumulation of dust column density with increasing distance, looking almost directly along the Carina Arm. In addition, our more limited latitude coverage at these longitudes may be implicated in the contradictory association of a long sightline with the lowest extinction bin (see Fig. 17). The lower overall density of candidate objects nearer the tangent direction may also be a clue that a more rapid accumulation of dust column brings the accessible sightlines more often than not to an end within the Arm. In effect, the view rarely reaches much beyond Westerlund 2 at $D \sim 6$ kpc (Dame 2007). This stands in contrast to the general vicinity of NGC 3603 (understood to be ~7 kpc distant: Sung & Bessell 2004), where it appears from

panel (c) in Fig. 18 that OB stars are being picked up at heliocentric distances up to ~10 kpc.

Our mapping can be compared with the *K*-band mapping carried out by Marshall et al. (2006) who produced a three-dimensional extinction map of the Milky Way by comparing empirical colours of giant stars in 2MASS with the expected intrinsic colours from the Besançon stellar population synthesis model. The angular resolution of this IR map is $0°.25$. Fig. 19 shows the derived extinction from Marshall et al. (2006) for 31-deg^2 patches falling within the region under examination here. The sightlines shown in blue correspond to the higher Galactic longitude side of the region containing NGC 3603 ($290°.5 < \ell < 291°.5$ and $-1° < b < 0°$), while those shown in red fall closest to the Carina tangent direction ($282°.5 < \ell < 283°.5$ and $-1° < b < 0°$). The lines shown in green pick out a region in between ($285°.5 < \ell < 286°.5$ and $-1° < b < 0°$). The conversion factor between A_K and A_0 is somewhat dependent on R_V: for the present purpose, we will use eight, appropriate for $R_V \sim 3.8$, to scale A_K up to A_0.

We overplot on the converted Marshall et al. (2006) relations in Fig. 19 the extinction-distance trends already presented in panels (c) and (d) of Fig. 18. The diamonds represent the lower longitude end of the footprint, while the triangles show the higher longitude end. Here we can see that the pattern apparent in the Marshall et al. (2006) data at $\ell \sim 291°$ is consistent with our data (the blue curves and triangles). On the other hand, the chaos in the OB-star data at lower longitudes (nearer the tangent, diamonds in the diagram), relative to the IR-based green and red curves, is underlined. In the remaining discussion, we restrict attention to the ordered behaviour seen at $\ell > 287°.6$.

We now evaluate how the OB-star defined mid-plane, as specified by the fit parameter, b_0, deviates from the geometrically flat mid-plane, at latitude b_m, along the observed pencil beam. The fit results relevant to this are collected together in Table 4. The parameter, b_m, is itself subject to some uncertainty as it depends both on D and the assumed height of the Sun the ideal flat mid-plane. To complete our calculation, we adopt estimates for b_m that follow from the prescription set out by Goodman et al. (2014), in which the Sun is offset above the mid-plane by 25 pc. The picture emerging from this is of a slowly growing offset, such that at ~7 kpc, the OB-star layer is about 60 pc below the geometric mid-plane, falling further to 80–100 pc below the heliocentric distances of 9–10 kpc. At $\ell \sim 290°$, this heliocentric distance range corresponds to a Galactocentric distance of ~10 kpc. The uncertainties in the estimates of warp in Table 4 arise only from the computed fit errors in the distance-extinction trend shown in Fig. 18: these are likely to be optimistic. In particular, the estimated distance scale carries an as yet unknown bias due to the potentially simplifying assumption – implicit in the fit procedure – that the average rise in A_0 with distance has no strong latitude dependence near the mid-plane.

Neutral hydrogen 21-cm line observations of the Galactic gas disc imply little warping of the Galactic plane out to Galactocentric radii of $R_G \sim 9$ kpc (Kalberla & Kerp 2009). What we see here – evidence of just the beginnings of a negative slowly growing warp – fits in with this. Well beyond $R_G = 9$ kpc, they and Levine, Blitz & Heiles (2006) propose a rapid increase in the warp such that an offset of ~500 pc is reached at a Galactocentric distance of $R_G \sim 15$ kpc.

6 DISCUSSION AND CONCLUSIONS

In this paper, we applied our a method for the uniform and high-efficiency selection of OB stars and parametrization of their extinc-tion, which was first laid out and validated by Mohr-Smith et al. (2015). The selection here, using VPHAS+ and 2MASS survey data, has resulted in a catalogue of 14 900 stars, of which 5915 are high-confidence O–B2 stars, drawn from 42 deg^2 in the Carina Arm region. The probable O stars number 905. The region charted here spans ~11° in Galactic longitude running from $\ell \sim 282°$, close to the Carina Arm tangent direction, to $\ell \sim 293°$, beyond the much studied massive cluster NGC 3603. By reaching down to $g = 20$ mag, roughly an order of magnitude increase is achieved relative to the numbers of known and candidate O–B2 stars brighter than ~12th magnitude: Reed (2003) lists 845 confirmed/probable O and early-B stars in the same sky area, while the spectroscopic cata-logue due to Maíz Apellániz et al. (2016) lists 106 O stars. Previous catalogues have included stars in the crowded hearts of NGC 3603 and Westerlund 2 that are missed here due to image blending. For example, Melena et al. (2008) reported 51 OB stars in the brilliant and packed ~10 arcsec core of NGC 3603 – our catalogue lists 17 of them. This illustrates the complementarity that exists between focused studies and wide-field survey selection.

By bringing together VPHAS+ u, g, r, i photometry with 2MASS J, H, K photometry, we are able to determine both the value of the extinction, A_0, and the extinction law, as parametrized by R_V, to good precision: both are typically measured to ~0.1 (magnitudes in the case of A_0). Using a statistically much larger sample across a large area on the sky, we have confirmed and fleshed out previous results, reported by many authors, that sightlines into the Carina Arm require flatter reddening laws with $3.5 \lesssim R_V \lesssim 4.0$ for $A_0 > 2.0$. Analysis in Section 5.3 has also demonstrated that extinction builds more quickly at Galactic longitudes closer to the Carina Arm tangent direction, where CO surface brightness is also known to rise to an evident peak (Grabelsky et al. 1987). Indeed at $\ell \lesssim 286°$, $g = 20$ is not yet deep enough to guarantee sightlines that pass through the Arm to much beyond a distance of 6–7 kpc. However, at greater longitudes, where the extinction builds at a mean rate of ~0.8 mag kpc^{-1}, the distances sampled extend beyond ~10 kpc (or R_G of at least 10 kpc also).

A crude impression of stellar effective temperatures (and hence distance moduli) is all that should be presumed to flow from the SED fits to the OnIR photometry of individual objects. How-ever, it is indeed possible to achieve a reasonable separation be-tween candidate O and candidate early-B stars. This was clearly confirmed in Section 4 where the analysis of AAOmega spec-troscopy of a representative sample of 276 OB candidates was presented. Among the better quality candidate objects ($\chi^2 < 7.82$), the cross-over rate, post-spectroscopy, at the O/B boundary was only 10–20 per cent (the higher percentage applying on the O star side of the boundary). We also showed that the systematic offset between the photometric and spectroscopic effective temperature scales has only a modest effect on the derived extinction param-eters for the B stars ($A_0 \sim +0.09$ and $R_V \sim -0.07$) and even less of an effect on the O stars ($A_0 \sim +0.03$ and $R_V s \sim -0.03$). This is a reflection of the convergence of the O star SED on to the Rayleigh–Jeans limit as effective temperature rises upwards of ~30 000 K. The follow-up spectroscopy demonstrated very clearly that there are very low levels of contamination from late-type stars within the selection (under 5 per cent of the accepted $\chi^2 < 7.82$ candidates).

Further exploitation of the parameters derived from the photome-try has also enabled an approximate distinction to be drawn between MS massive OB stars and lower luminosity hot stars (sub-dwarfs, post-AGB stars and others), and higher luminosity evolved mas-sive OB stars. Intriguingly, the one sub-luminous candidate to be
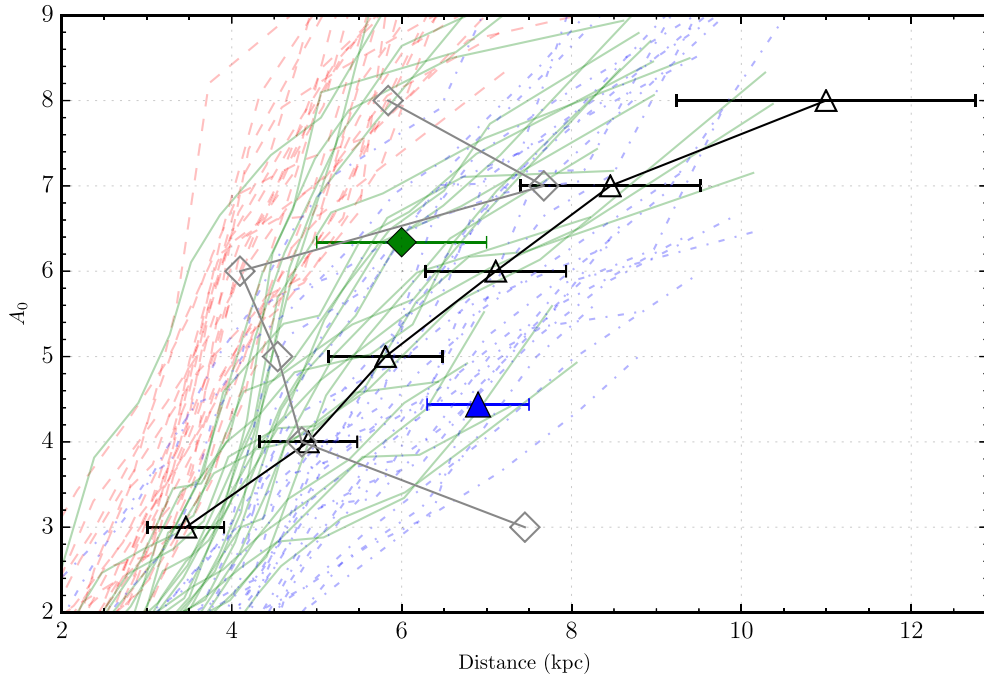
Figure 19. Comparison of the derived values of extinction as a function of distance between Marshall et al. (2006) and this study. The diamonds show the end of the footprint closer to the Carina Arm tangent, while the triangles show the opposite end around NGC 3603 (selections as in Fig. 18). Error bars are included for the more credible longer longitude sample (panel c in Fig. 18). The red dashed lines and the blue dot–dashed lines are selections from Marshall et al. (2006), each sampling a square degree around, respectively, $\ell = 283°$, $b = -0°.5$ and $\ell = 291°$, $b = -0°.5$, at opposite ends of the footprint studied in this paper. The solid lines shown in green correspond to a square degree around $\ell = 286$, $b = -0°.5$, near Wd 2. The blue triangle and green diamond show the corresponding values for NGC 3603 and Wd 2, respectively.

followed up spectroscopically has emerged as a helium-enriched probable post-AGB object: the helium enrichment, in particular, is suggestive of material dredged up in a late helium flash. The narrow-band Hα filter in the VPHAS+ survey offers a clear path to the selection of emission-line objects and we find a fraction of B-type emission-line stars (~7 per cent) relative to the total B population that is consistent with the southern clusters study by McSwain & Gies (2005). The majority of emission-line candidates are likely to be classical Be stars, while a minority may also be examples of B[e] stars, luminous blue variables or WR stars. The high-confidence broad-band selection tends to disproportionately exclude new WR stars and many CBe stars for the reason that these objects often present with NIR excesses that lead to inferior ($\chi^2 > 7.82$) SED fits.

The catalogue created by this study is an opportunity to explore how a high-angular resolution wide-field optical survey like VPHAS+ can bring a wider context to the study of star-forming regions, away from the dense well-studied cores of open clusters and OB associations. The capability is now there to identify massive stars, wherever they are. A compelling example of this is the very large number of candidate reddened O stars lying in an extended halo around the brilliant cluster, NGC 3603 at Galactic coordinates (291.6, −0.5). This can be seen in Fig. 20 that shows the distribution of candidate O stars ($\log(T_{\rm eff}) > 4.477$) on their own across the whole region. Many objects are seen around NGC 3603, spread across a sky area about a degree across – we find around 500 high-confidence O–B2 candidates in the extinction range $4.0 < A_0 < 7.0$, of which more than 100 are probable O stars. Very recently, Roman-Lopes, Franco & Sanmartim (2016) have used NIR selection to identify 10 candidate early-O stars in this same region and have confirmed them spectroscopically: all are in our catalogue with

$\log(T_{\rm eff})$ and A_0 parameters from SED fitting that are very close to their spectroscopic counterparts. The shape on-sky of the O star surface density enhancement fits in well with 'star-forming complex #28', one of two G291 regions, identified via long-wavelength free–free emission by Rahman & Murray (2010). Metaphorically speaking, NGC 3603 is the tip of a massive-star iceberg worthy of further investigation.

In Section 5.2, we also saw that at $\ell = 289°.77$, $b = -1°.22$, there is a clustering of OB stars in the vicinity of the bright O5 supergiant, LSS 2063, which, before now, had evaded optical detection and cataloguing. This is sufficiently dispersed to be viewed as an OB association. As a further example, Fig. 20 contains hints of another dispersed OB complex at $\ell \simeq 283°$ and $b \simeq -0°.5$: in view of the similarly high extinctions involved ($A_0 \gtrsim 6$), it is likely to be about as distant as Westerlund 2.

Many of the already well-known O stars in the Carina Nebula/Carina OB1 association at $l \sim 288°$ are missing from the selection presented here because they are brighter than our bright selection limit (at $V \sim 12$). However, we do sweep up a handful of O star candidates and many B star candidates (see Fig. 17) which are far more extinguished than the typical values of $A_V \sim 2.5$ of known clusters such as Trumpler 14 and 16 (Hur et al. 2012). Our objects are likely to be situated behind or deeper into the nebula than the well-studied cluster stars. Indeed, the closest distance for the majority of massive OB stars in the catalogue presented here is expected to be 2.5–3 kpc, the range in distance within which the Carina Nebula is likely to be located.

The full catalogue of blue selected objects, including spectroscopic data where they exist, is available in machine-readable form as supplementary material and will also become available via Centres de Données astronomique de Strasbourg (CDS): the Appendix
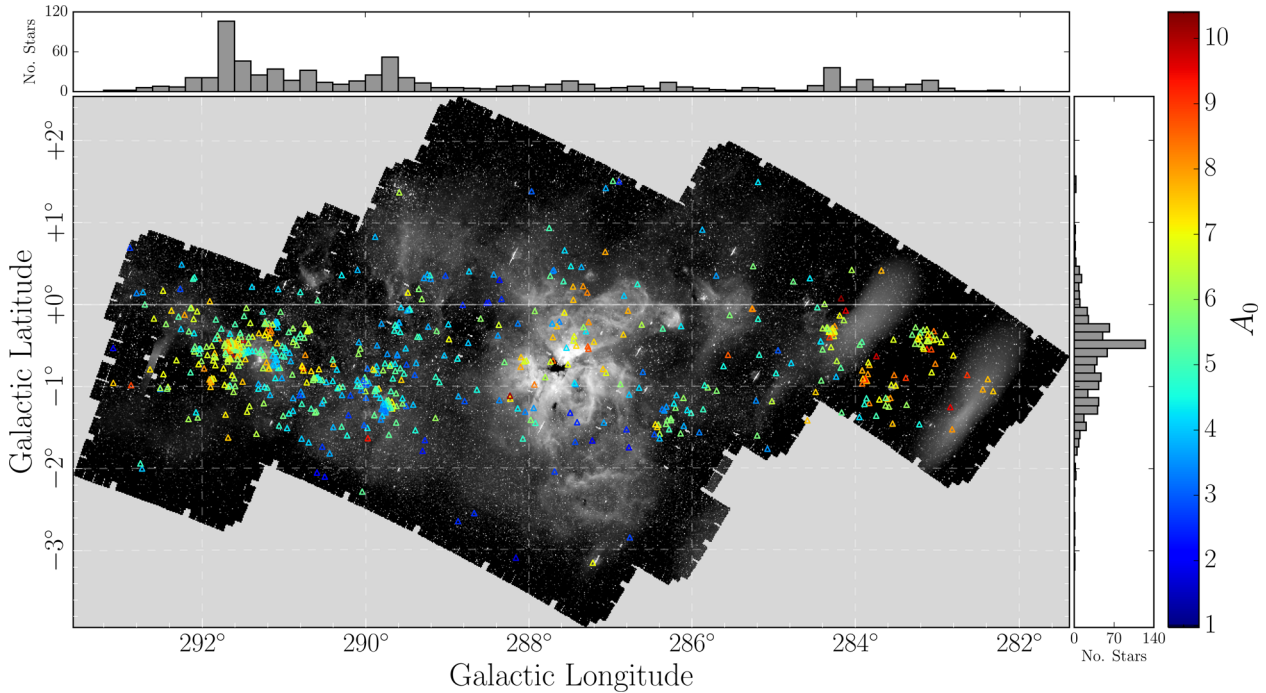
Figure 20. Spatial distribution of candidate O stars across the Carina region, coloured according to extinction, A_0. The histograms above and to the right of the plot show the Galactic longitude and latitude distributions, respectively.

to this paper provides a specification of the columns making up the catalogue.

The ability to efficiently and reliably select and measure thousands of fainter OB stars opens the way to using these intrinsically luminous objects to probe the structure of the Galactic disc in a more fine-grained fashion than has been possible before. Through sampling the field thoroughly, for the first time, as well as massive star clusters, this study has provided systematic evidence that the latter promote somewhat flatter optical extinction laws (i.e. increased R_V) alongside greater A_0. The results of Fitzpatrick & Massa (2007, fig. 11) hint at this but lack the sampling in the field. The Carina Nebula itself has emerged as an especially striking example of raised R_V. Around NGC 3603, we obtain a median extinction of 6 mag and median $R_V \simeq 3.75$, to be compared with below 5 and 3.55 mag, respectively, recently measured inside the cluster (Pang, Pasquali & Grebel 2016). Further investigation of the subtle differentiations beginning to appear may help fill out the picture of dust processing arising from star formation.

The Galactic latitude distribution of the OB stars has been shown to imply incipient disc warping along sightlines near $\ell = 290°$: our approximate method of inferring distance via reddening suggests heliocentric distances of the order of 10 kpc are reached and that the OB-star layer offset below the mid-plane at this distance is likely to be 80–100 pc (Section 5.3). Before now, similar efforts using OB stars to trace disc warping have had to work with very much lower sky densities of bright objects (1300 stars over a third of the Galactic disc; Reed 1996) or accept data inhomogeneity (600 Carina region stars compiled from four catalogues; Kaltcheva & Scorcio 2010). These authors and Graham (1970) proposed stronger warping, compared to the new result, in part because of overestimation of distances driven by underestimation of visual extinctions (through the adoption of $R_V \simeq 3.1$).

The deep census provided here will be extended across the rest of the Galactic plane in future publications as VPHAS+, along with

its northern counterparts, The INT/WFC Photometric Hα Survey (Drew et al. 2005) and The UV Excess Survey (Groot et al. 2009) progress to fully calibrated completion. These are set to combine transformationally with forthcoming *Gaia* astrometry – reaching to a similar faint limit – in enabling much more precise analysis both of Galactic disc structure and also of the ecology and life cycles of massive Galactic clusters and their environments.

REFERENCES

Allen T. S., Prchlik J. J., Megeath S. T., Gutermuth R. A., Pipher J. L., Naylor T., Jeffries R. D., 2014, ApJ, 786, 113
Astropy Collaboration, et al., 2013, A&A, 558, A33
Avedisova V. S., 2002, Astron. Rep., 46, 193
Bailer-Jones C. A. L., 2011, MNRAS, 411, 435
Bertelli G., Bressan A., Chiosi C., Fagotto F., Nasi E., 1994, A&AS, 106, 275
Bobylev V. V., Bajkova A. T., 2016, Astron. Lett., 42, 1
Bressan A., Marigo P., Girardi L., Salasnich B., Dal Cero C., Rubele S., Nanni A., 2012, MNRAS, 427, 127
Bressert E. et al., 2012, A&A, 542, A49
Cardelli J. A., Clayton G. C., Mathis J. S., 1989, ApJ, 345, 245
Caswell J. L., Haynes R. F., 1987, A&A, 171, 261
Conti P. S., Vacca W. D., 1990, AJ, 100, 431
Crowther P. A., Lennon D. J., Walborn N. R., 2006, A&A, 446, 279
Dame T. M., 2007, ApJ, 665, L163
Dame T. M., Hartmann D., Thaddeus P., 2001, ApJ, 547, 792
de Wit W. J., Testi L., Palla F., Zinnecker H., 2005, A&A, 437, 247
Draine B. T., 2011, ApJ, 732, 100
Drew J. E. et al., 2005, MNRAS, 362, 753
Drew J. E. et al., 2014, MNRAS, 440, 2036
Dutra C. M., Bica E., Soares J., Barbuy B., 2003, A&A, 400, 533
Evans C. J. et al., 2011, A&A, 530, A108
Faherty J. K., Shara M. M., Zurek D., Kanarek G., Moffat A. F. J., 2014, AJ, 147, 115
Fitzpatrick E. L., Massa D., 2007, ApJ, 663, 320
Foreman-Mackey D., Hogg D. W., Lang D., Goodman J., 2013, PASP, 125, 306
Garmany C. D., Conti P. S., Chiosi C., 1982, ApJ, 263, 777
Georgelin Y. M., Russeil D., Amram P., Georgelin Y. P., Marcelin M., Parker Q. A., Viale A., 2000, A&A, 357, 308
Goodman A. A. et al., 2014, ApJ, 797, 53
Grabelsky D. A., Cohen R. S., Bronfman L., Thaddeus P., May J., 1987, ApJ, 315, 122
Graham J. A., 1970, AJ, 75, 703
Green E. M., Fontaine G., Hyde E. A., For B.-Q., Chayer P., 2008, in Heber U., Jeffery C. S., Napiwotzki R., eds, ASP Conf. Ser. Vol. 392, Hot Subdwarf Stars and Related Objects. Astron. Soc. Pac., San Francisco, p. 75
Groot P. J. et al., 2009, MNRAS, 399, 323
Han Z., Podsiadlowski P., Maxted P. F. L., Marsh T. R., 2003, MNRAS, 341, 669
Huang W., Gies D. R., McSwain M. V., 2010, ApJ, 722, 605
Hur H., Sung H., Bessell M. S., 2012, AJ, 143, 41
Johnson H. L., Morgan W. W., 1953, ApJ, 117, 313
Kalberla P. M. W., Kerp J., 2009, ARA&A, 47, 27
Kaltcheva N., Scorcio M., 2010, A&A, 514, A59
Kroupa P., 2001, MNRAS, 322, 231
Kumar B., Sharma S., Manfroid J., Gosset E., Rauw G., Nazé Y., Kesh Yadav R., 2014, A&A, 567, A109
Langer N., 2012, ARA&A, 50, 107
Lanz T., Hubeny I., 2003, ApJS, 146, 417
Lanz T., Hubeny I., 2007, ApJS, 169, 83
Levine E. S., Blitz L., Heiles C., 2006, ApJ, 643, 881
McSwain M. V., Gies D. R., 2005, ApJS, 161, 118

Maíz Apellániz J., Sota A., Walborn N. R., Alfaro E. J., Barbá R. H., Morrell N. I., Gamen R. C., Arias J. I., 2011, in Zapatero Osorio M. R., Gorgas J., Maíz Apellániz J., Pardo J. R., Gil de Paz A., eds, Highlights of Spanish Astrophysics VI. p. 467
Maíz Apellániz J. et al., 2014, A&A, 564, A63
Maíz Apellániz J. et al., 2016, ApJS, 224, 4
Maíz-Apellániz J., Walborn N. R., Galué H. Á., Wei L. H., 2004, ApJS, 151, 103
Majaess D., 2013, Ap&SS, 344, 175
Markova N., Puls J., Simón-Díaz S., Herrero A., Markov H., Langer N., 2014, A&A, 562, A37
Marshall D. J., Robin A. C., Reylé C., Schultheis M., Picaud S., 2006, A&A, 453, 635
Martins F., Plez B., 2006, A&A, 457, 637
Martins F., Schaerer D., Hillier D. J., 2005, A&A, 436, 1049
Melena N. W., Massey P., Morrell N. I., Zangari A. M., 2008, AJ, 135, 878
Meylan G., Maeder A., 1983, A&A, 124, 84
Mohr-Smith M. et al., 2015, MNRAS, 450, 3855
Napiwotzki R., 1999, A&A, 350, 101
Nieva M.-F., 2013, A&A, 550, A26
Ochsendorf B. B., Tielens A. G. G. M., 2015, A&A, 576, A2
Paladini R., Davies R. D., De Zotti G., 2004, MNRAS, 347, 237
Pang X., Pasquali A., Grebel E. K., 2011, AJ, 142, 132
Pang X., Pasquali A., Grebel E. K., 2016, AJ, 151, 23
Planck Collaboration XI , 2014, A&A, 571, A11
Portegies Zwart S. F., McMillan S. L. W., Gieles M., 2010, ARA&A, 48, 431
Povich M. et al., 2011, ApJS, 194, 6
Puls J., Urbaneja M. A., Venero R., Repolust T., Springmann U., Jokuthy A., Mokiem M. R., 2005, A&A, 435, 669
Raddi R., Drew J. E., Steeghs D., Wright N. J., Drake J. J., Barentsen G., Fabregat J., Sale S. E., 2015, MNRAS, 446, 274
Rahman M., Murray N., 2010, ApJ, 719, 1104
Rauch T., Heber U., Werner K., 2002, A&A, 381, 1007
Reed B. C., 1996, AJ, 111, 804
Reed B. C., 2000, AJ, 120, 314
Reed B. C., 2003, AJ, 125, 2531
Roman-Lopes A., Franco G. A. P., Sanmartim D., 2016, ApJ, 823, 96
Russeil D., 2003, A&A, 397, 133
Schmidt-Kaler T., 1982, Landolt-Börnstein: Numerical Data and Functional Relationships in Science and Technology - New Series. Springer-Verlag, Berlin
Simón-Díaz S., Herrero A., 2014, A&A, 562, A135
Simón-Díaz S., Castro N., Garcia M., Herrero A., Markova N., 2011, Bull. Soc. R. Sci. Liege, 80, 514
Stark M. A., Wade R. A., 2003, AJ, 126, 1455
Sung H., Bessell M. S., 2004, AJ, 127, 1014
Tan J. C., Beltrán M. T., Caselli P., Fontani F., Fuente A., Krumholz M. R., McKee C. F., Stolte A., 2014, in Beuther H., Klessen R. S., Dullemond C. P., Henning T., eds, Protostars and Planets VI. Univ. Arizona Press, Tucson, AZ, p. 149
Tapia M., Roth M., Vázquez R. A., Feinstein A., 2003, MNRAS, 339, 44
Taylor M. B., 2005, in Shopbell P., Britton M., Ebert R., eds, ASP Conf. Ser. Vol. 347, Astronomical Data Analysis Software and Systems XIV. Astron. Soc. Pac., San Francisco, p. 29
Vallée J. P., 2014, AJ, 148, 5
Walborn N. R., Fitzpatrick E. L., 2000, PASP, 112, 50
Wramdemark S., 1976, A&AS, 23, 231
Wright E. L. et al., 2010, AJ, 140, 1868
Zorec J., Briot D., 1997, A&A, 318, 443

SUPPORTING INFORMATION

Supplementary data are available at *MNRAS* online.

Table A1. Specifications for all the columns in the data base provided in the supplementary materials.

Figure 17. An animation showing how the on-sky distribution of OB stars modifies with increasing extinction, A_0. O stars and early-B stars are represented as triangles and circles, respectively. The histogram to the right shows the full distribution of stars in A_0, while the sliding bar on the colour scale identifies the reddening range displayed at every instant. The printed version of this figure picks out the OB star distribution for three distinct A_0 ranges.

Please note: Oxford University Press is not responsible for the content or functionality of any supporting materials supplied by the authors. Any queries (other than missing material) should be directed to the corresponding author for the article.

APPENDIX A: DATABASE DESCRIPTION

The catalogue of the complete set of 14 900 candidate OB stars selected from the VPHAS+ ($u - g$, $g - r$) colour–colour diagram is provided as a machine-readable data base in the supplementary material. This will be made available via CDS.

The source positions and multiband photometry on which the initial selection was made is provided in the first 17 columns. The RA and Dec. reported are derived from the r-band observations obtained with the u and g filters. Columns 18–24 list the 2MASS cross-match magnitudes and errors: note that the data base does not include blue-selected objects without 2MASS counterparts. All photometric magnitudes are reported in the Vega system. For 152 (~1 per cent) of the selected objects, Hα magnitudes are presently unavailable: where this applies the data base entry is left blank. Similarly, the second r magnitude is missing for 59 stars. Column 24 lists the VPHAS+/2MASS cross-match separation.

The next columns, 25–38, summarize the results of the SED fits, presenting the median of the posterior distribution for all four parameters along with errors derived from the 16th and 84th percentiles (essentially 1σ errors). The final important piece of information from the fits is the value of χ^2 computed for the best-fitting SED, given in column 37: where this value is <7.82 and $\log(T_{\rm eff}) > 4.30$ (to two significant figures), column 38 in the data base is set to true. We caution that the parameters for objects with $\chi^2 > 7.82$ are less reliable: these objects are more heterogeneous and will include emission-line objects, some normal OB stars as well as contaminant objects. Columns 39–41 are similar boolean columns that identify candidate emission-line stars (as determined from $(r - H\alpha)$ excess) and sub-luminous and evolved non-MS OB candidates.

Where alternative names for an object already exist in the SIM-BAD data base, we write this into column 42, the 'Notes' column. We also note any other specific characteristics of the object that have already come to attention: in particular, if an AAOmega spectrum exists that shows the object to have line emission at Hβ, we note it here. The small number of known contaminant late-type stars are noted here also.

The final set of columns (43–53) records whether an AAAOmega spectrum exists and reports numerical quantities derived from model atmosphere fits as appropriate. For the contaminant stars, all numerical quantities are omitted.

Table A1 below provides individual specifications for all the columns in the data base.

Table A1. Specifications for all the columns in the data base provided in the supplementary materials.

Column	Name	Description	Units	Type
1	Name	'VPHAS_OB1_NNNNN', where 'NNNNN' is ordered by Galactic longitude		String
2	RA	Right Ascension (J2000)	Deg.	Float
3	Dec.	Declination (J2000)	Deg.	Float
4	GAL_LONG	IAU 1958 Galactic longitude	Deg.	Float
5	GAL_LAT	IAU 1958 Galactic latitude	Deg.	Float
6	u	VPHAS+ u-band	Vega mag	Float
7	u_err	VPHAS+ u-band photometric uncertainty	Vega mag	Float
8	g	VPHAS+ g-band	Vega mag	Float
9	g_err	VPHAS+ u-band photometric uncertainty	Vega mag	Float
10	r	VPHAS+ r-band taken with u and g (used in SED fits)	Vega mag	Float
11	r_err	VPHAS+ r-band photometric uncertainty	Vega mag	Float
12	r2	VPHAS+ second r band, taken with i and Hα	Vega mag	Float
13	r2_err	VPHAS+ second r-band photometric uncertainty	Vega mag	Float
14	i	VPHAS+ i band	Vega mag	Float
15	i_err	VPHAS+ i-band photometric uncertainty	Vega mag	Float
16	Ha	VPHAS+ Hα band	Vega mag	Float
17	Ha_err	VPHAS+ Hα band photometric uncertainty	Vega mag	Float
18	J	2MASS J band	Vega mag	Float
19	J_err	2MASS J-band photometric uncertainty	Vega mag	Float
20	H	2MASS H band	Vega mag	Float
21	H_err	2MASS H-band photometric uncertainty	Vega mag	Float
22	K	2MASS K band	Vega mag	Float
23	K_err	2MASS K-band photometric uncertainty	Vega mag	Float
24	xmatch_r	The cross-match distance between VPHAS+ and 2MASS	arcseconds	Float
25	logTeff	Estimated effective temperature from photometric fits (median of posterior)	log(K)	Float
26	logTeff_eu	Upper uncertainty on logTeff (84th percentile of posterior)	log(K)	Float
27	logTeff_el	Lower uncertainty on logTeff (16th percentile of posterior)	log(K)	Float
28	A0	Estimated extinction, A_0, from photometric fits (median of posterior)	mag	Float
29	A0_eu	Upper uncertainty on A_0 (84th percentile of posterior)	mag	Float
30	A0_el	Lower uncertainty on A_0 (16th percentile of posterior)	mag	Float
31	Rv	Estimated extinction law parameter, R_V, from photometric fits (median of posterior)		Float
32	Rv_eu	Upper uncertainty on RV (84th percentile of posterior)		Float
33	Rv_el	Lower uncertainty on RV (16th percentile of posterior)		Float
34	mu	Estimated distance modulus, μ, from photometric fits (median of posterior)	mag	Float
35	mu_eu	Upper uncertainty on mu (84th percentile of posterior)	mag	Float
36	mu_el	Lower uncertainty on mu (16th percentile of posterior)	mag	Float
37	chi2	χ^2 value for photometric fit		Float
38	goodOB	Indicates if object has $\chi^2 < 7.82$ and $\log(T_{\rm eff}) > 4.30$, rounded to significant figures		Boolean
39	EM	Indicates if star is selected as an emission-line object		Boolean
40	SUB	Indicates if star is selected as a sub-luminous object		Boolean
41	LUM	Indicates if star is selected as an overluminous object		Boolean
42	Notes	Comments, including SIMBAD cross-identification name where it exists		String
43	SPEC	Indicates if star has an AAOmega spectrum		Boolean
44	spec_mod	The model grid used for fitting: TLUSTY or FASTWIND		String
45	speclogTeff	Estimated effective temperature derived from spectroscopic fit (median of posterior)	log(K)	Float
46	speclogTeff_eu	Upper uncertainty on specTeff (84th percentile of posterior)	log(K)	Float
47	speclogTeff_el	Lower uncertainty on specTeff (16th percentile of posterior)	log(K)	Float
48	logg	Estimated surface gravity derived from spectroscopic fits (median of posterior)	dex	Float
49	logg_eu	Upper uncertainty on log g (84th percentile of posterior)	dex	Float
50	logg_el	Lower uncertainty on log g (16th percentile of posterior)	dex	Float
51	vsinsi	Estimated rotational velocity derived from spectroscopic fits (median of posterior)	kms^{-1}	Float
52	vsini_eu	Upper uncertainty on $v \sin i$ (84th percentile of posterior)	kms^{-1}	Float
53	vsini_el	Lower uncertainty on $v \sin i$ (16th percentile of posterior)	kms^{-1}	Float

This paper has been typeset from a TeX/LaTeX file prepared by the author.